ESD TDR 64-37
ESTI FILE COPY

ESD-TDR-64-37

Technical Report 349

Radar Scattering from a Conducting Cone-Sphere

J. H. Pannell
J. Rheinstein
A. F. Smith

2 March 1964

Prepared under Electronic Systems Division Contract AF 19(628)-500 by

Lincoln Laboratory
MASSACHUSETTS INSTITUTE OF TECHNOLOGY
Lexington, Massachusetts

ESD RECORD COPY
RETURN TO
SCIENTIFIC & TECHNICAL INFORMATION DIVISION
(ESTI), BUILDING 1211
COPY NR _____ OF _____ COPIES

ESTI PROCESSED
☐ DDC TAB ☐ PROJ OFFICER
☐ ACCESSION MASTER FILE
☐ _____
JUN 10 1964
DATE _____
ESTI CONTROL NR AL 40655
CY NR 1 OF 1 CYS

AD0600411

The work reported in this document was performed at Lincoln Laboratory, a center for research operated by Massachusetts Institute of Technology, with the support of the U.S. Air Force under Contract AF 19(628)-500.

Non-Lincoln Recipients

PLEASE DO NOT RETURN

Permission is given to destroy this document when it is no longer needed.

MASSACHUSETTS INSTITUTE OF TECHNOLOGY

LINCOLN LABORATORY

RADAR SCATTERING FROM A CONDUCTING CONE-SPHERE

J. H. PANNELL

J. RHEINSTEIN

A. F. SMITH

Group 22

TECHNICAL REPORT 349

2 MARCH 1964

LEXINGTON MASSACHUSETTS

ABSTRACT

As part of an investigation of the radar backscatter properties of axisymmetric conducting shapes, a study has been made of backscattering by a cone-sphere. This body is comprised of a circular cone with a 25° included cone angle, terminated by a tangent spherical segment. Measurements of backscatter cross sections over all aspect angles are presented for wavelengths in the range from one-tenth to twice the radius of the spherical segment. Comparison of measured values with theoretical predictions shows that satisfactory agreement is obtained for all aspect angles.

This technical documentary report is approved for distribution.

Franklin C. Hudson, Deputy Chief
Air Force Lincoln Laboratory Office

TABLE OF CONTENTS

	Abstract	iii
I.	INTRODUCTION	1
	A. Background Information	1
	B. Effect of Shape on Scattering Properties	1
II.	MEASUREMENTS	3
III.	BACKGROUND RETURN	5
IV.	RESULTS	5
	A. Nose-On Region	5
	B. Cone Specular Reflection	10
	C. Sphere Specular Reflection	10

RADAR SCATTERING FROM A CONDUCTING CONE-SPHERE

I. INTRODUCTION

A. Background Information

An intriguing problem in radar scattering is reduction of the radar backscatter cross section of a large body. Two approaches to the problem may be followed: one employs techniques or substances that absorb the incident energy; the other employs methods that redirect the energy so that scattering occurs in directions other than toward the receiver. The problem being considered here is backscatter, where the receiver and transmitter are collocated. One example of the second approach, based on refraction, was the Eaton Lens, but that turned out to be unpromising.[1] On the other hand, shaping the body, so that in some preferred orientation back-reflections are minimized, has been demonstrated to be of considerable value. It was the objective of the study reported here to determine, for one of the simplest of these streamlined shapes, the cone-sphere, what mechanisms limited the minimum attainable cross section. This was to be accomplished by the correlation of the results of backscattering measurements over a wide range of the body-size-to-wavelength ratio with the best attainable theoretical predictions.

B. Effect of Shape on Scattering Properties

The discussion in this section is concerned with backscattering from axisymmetric "teardrop" shapes with one end sharply pointed (the "nose") and the other end smoothly rounded. The aspect angle ψ is the angle between the body axis and the direction for which backscatter is under consideration; it has the value zero when the incident wave is directed along the body axis toward the pointed end (Fig. 1).

For these shapes, no specular backscattering occurs at aspect angles near zero (often referred to as the "nose-on" region). The backscattering that does occur in this region is believed to arise from the contributions of three mechanisms:

(1) Tip scattering: diffraction by the pointed nose of the body; this would be the only contribution present for a cone of infinite length.

(2) Traveling waves: reflections of surface waves by surface derivative discontinuities; e.g., a simple right circular cone would show a gross effect because of the edge.

(3) Creeping waves: radiation from surface waves that may be thought of as traveling around the rear or shadowed region and spraying back at the observer.

The simplest shape in which specular reflections and edge effects are suppressed, and one which has received much consideration,[2] is the cone-sphere combination consisting of a circular

TABLE I

MEASUREMENT PARAMETERS

Measuring Agency	Model Material	a/λ	Measurement Frequency (Mcps)	Polarization
DRTE	Magnesium	1.47	9,000	HH [$d = 2.4(D^2/\lambda)$] HH [$d = 1.5(D^2/\lambda)$] VV
		5.70	35,000	HH VV
RAT SCAT	Silver-coated balsa	2.4	2,200	HH VV
Radiation, Inc.	Aluminum	1.57	9,600	HH VV
	Silver-coated epoxy	3.91	9,600	HH VV
	Silver-coated balsa	0.60	550	HH VV
		1.45	1,335	HH VV
		6.09	5,600	HH VV
		10.43	9,600	HH VV

cone terminated by a tangent spherical cap of radius a. This is illustrated in Fig. 1. The conical forebody prevents specular backscatter for aspect angles within $(90 - \alpha)$ degrees of nose-on, where α is the cone half-angle. In addition, there are no discontinuities in the first surface derivative, other than at the tip, and the backscatter due to the tip is, in general, negligible in comparison with return from other sources.

There is, however, a discontinuity in the second surface derivative (or, in what is essentially the same, the curvature of the surface) at the junction of the cone and the spherical cap. This does contribute a so-called traveling wave return. When the wavelength of the incident radiation is less than about one-third of the radius of the spherical cap and for cone half-angles less than about 20°, the traveling wave component appears to be the principal contributor to the backscattering at near nose-on incidence. At longer wavelengths the creeping wave appears to contribute the largest return (as shown in Fig. 26).

II. MEASUREMENTS

Radar backscatter measurements have been obtained on various models of the cone-sphere which were fabricated to give ratios of a/λ ranging from 0.60 to 10.43, the measurements being obtained at frequencies ranging from 550 to 35,000 Mcps as detailed in Table I.

Cross-section data were obtained at: the USAF facility "RAT SCAT," Holloman Air Force Base, New Mexico; Radiation, Inc., Melbourne, Florida; and the Defense Research Telecommunications Establishment (DRTE), Ottawa, Canada. The following paragraphs describe briefly the measurement technique used at each of these facilities.

Data were obtained on the outdoor ranges of RAT SCAT and Radiation, Inc., using pulsed radars at frequencies of 550, 1335, 2200, 5600, and 9600 Mcps. At DRTE's indoor range, data were obtained at 35,000 Mcps using a short pulse radar, and at 9000 Mcps using a CW balanced-bridge radar. All the models were supported by styrofoam columns with the model axes in or near a horizontal plane. The radar beam axis lay in the same plane. A transit was used for model alignment at RAT SCAT and at Radiation, Inc.; at DRTE the model was leveled using a transit, and an optical sighting system was used to locate the center of rotation of the model on the axis of the transmitting antenna.

The radars at RAT SCAT, at Radiation, Inc., and the DRTE K_a-band radar employed separate transmitting and receiving antennas, so that a small bistatic angle (of the order of 1°) is involved in these measurements. The DRTE X-band radar employed a single antenna for both transmitting and receiving. All models were measured with transmitting and receiving antennas polarized in a horizontal plane (HH polarization) and with both antennas polarized in a vertical plane (VV polarization).

The measurement distances d employed at RAT SCAT and at Radiation, Inc., were in all cases in excess of $2(D^2/\lambda)$ (where the dimension D is the larger of the antenna aperture and the model length, and λ is the wavelength of the transmitted radiation). At DRTE, the measurements at 9000 Mcps were made at a distance of 18 feet [$\approx 2.4(D^2/\lambda)$, where D is model length] with a duplicate set of measurements made at HH polarization at a distance of 11 feet [$\approx 1.5(D^2/\lambda)$]. At 35,000 Mcps, the measurement distance was 27 feet [$\approx 0.9(D^2/\lambda)$].

For each measurement run, the model was rotated through 360° about a vertical axis. Background (column) return (at least in the nose-on region and often through 360°) and the return from a calibration standard were recorded for each model measurement at RAT SCAT and at Radiation, Inc. Less extensive background records were obtained from DRTE.

TABLE II

MEASURED AND THEORETICAL DATA

Background Data						Model Data				Specular Return from Sphere
			Average Background Return Nose-On (±45°)		Average Cross-Section Return Nose-On (±45°)	Specular Return from Cone				
						Magnitude		Lobe Width		Average Cross Section (90° to 270°)
a/λ	Measured Frequency (Mcps)	Polarization	Before Model Measurement ($db\lambda^2$)	After Model Measurement ($db\lambda^2$)	($db\lambda^2$)	Measured ($db\lambda^2$)	Theoretical ($db\lambda^2$)	Measured (deg)	Theoretical (deg)	($db\lambda^2$)
0.60	550	HH	−28	−21	−12	12	12	20.8	21.2	3
		VV	−33	−23	−12	12		25.8		2
1.45	1,335	HH	−28	−26	−15	22	23	9.2	8.7	8
		VV	<−28	−20	−11	22		9.7		8
1.47	9,000	HH	*	*	−11	22	24	9.0	8.6	9
		HH	*	*	−14	20		9.3		8
		VV	*	*	−10	22		9.1		7
1.57	9,600	HH	<−22†	−22†	−14	25	24	8.0	8.1	11
		VV	*	−19†	−12	24		8.2		9
2.40	2,200	HH	*	−25	−13	30	30	5.8	5.4	14
		VV	*	−25	−11	31	30	5.7		14
3.91	9,600	HH	−25	−20‡	−15	37	36	3.1	3.2	18
		VV	−26	−26	−12	36		3.4		17
5.70	35,000	HH	*	*	−11	32	41	4.7	2.2	20
		VV	−10	*	−12	32		5.3		18
6.09	5,600	HH	<−17†	<−17†	−15	39	42	2.7	2.1	21
		VV	<−17†	<−16†	−15	40		2.3		19
10.43	9,600	HH	<−20	<−20‡	−5	47	49	1.7	1.2	25
		VV	−22	<−25‡	−5	46		1.4		24

* Data not available.

† Background return off chart in most regions.

‡ Average in region ± 20° from nose-on.

III. BACKGROUND RETURN

Measurements of the return from the background, including the supporting column were made both before and after each model measurement at Radiation, Inc., and after each measurement at RAT SCAT. Estimates of average background cross section in the region 0° to ±45° from nose-on have been made and are shown in Table II.

The less extensive background data available for the DRTE measurements are tabulated below in units of decibels with respect to a square wavelength.

(a) Frequency: 9000 Mcps

Column Level: $-40\ db\lambda^2$ at nose-on
$-29\ db\lambda^2$ at peaks
$-35\ db\lambda^2$ for 60 percent of tower rotation
$-30\ db\lambda^2$ for 20 percent of tower rotation
$-40\ db\lambda^2$ for 20 percent of tower rotation

(b) Frequency: 35,000 Mcps

Patterns of background return vs aspect angle were supplied for vertical polarization. An estimate of average background level at aspects ±45° from nose-on is $-10\ db\lambda^2$.

The principal contributor to background return is reflection from the styrofoam columns at DRTE and at RAT SCAT, selection and shaping of the column minimizes the return from it; at Radiation, Inc., an absorbing shield below the column is adjusted to obtain a minimum return by destructive interference; at RAT SCAT, the column can also be tilted back to reduce the return at selected aspect angles. Useful measurements require at least a factor of 10 (i.e., 10 db) between returns from target and from background (as shown in Fig. 22).

IV. RESULTS

Measurements were obtained on the metallic and silver painted models at a number of frequencies corresponding to values of the ratio a/λ ranging from 0.60 to 10.43. Data were obtained for both horizontal and vertical antenna polarizations; polar plots thereof are shown in Figs. 2 through 20, where all data have been plotted in units of decibels relative to λ^2. The characteristics of these patterns are discussed in the following paragraphs.

Where average cross-section values are quoted, these were calculated by a numerical integration (sampling interval <0.5°, and in general ~0.2° to 0.3°) of the cross section (in square wavelengths) over the interval indicated and then converted to decibels relative to one square wavelength.

A. Nose-On Region

1. Pattern Symmetry

For those patterns corresponding to higher values of a/λ, there is a lack of symmetry in the region ±70° from nose-on. For those patterns (Figs. 15 and 16) obtained at DRTE on the magnesium model at a measurement frequency of 35,000 Mcps ($a/\lambda = 5.7$), this asymmetry is probably attributable to high background return. As indicated above, the average background level over ±45° from nose-on for the measurement at vertical polarization (VV pol.) was approximately $-10\ db\lambda^2$; it may be assumed also that the background level for the horizontal polarization (HH pol.) measurement was about the same. The calculated averages over the same region for the model measurement (Table II) are $-11\ db\lambda^2$ (HH pol.) and $-12\ db\lambda^2$ (VV pol.),

which are lower than the average background level. Thus, interference between the background return and the model return probably accounts for the asymmetrical patterns obtained for these two measurements.

The other patterns showing asymmetrical behavior in the nose-on region are those obtained at 5600 and 9600 Mcps (Figs. 17 through 20) on a large model, giving values of 6.09 and 10.4 for a/λ, and those obtained at 9600 Mcps (Figs. 13 and 14) on a model giving a value of 3.91 for a/λ. In the measurements for $a/\lambda = 10.43$, the average background level was more than 15 db below the average model return in the region ±45° from nose-on. Thus, background interference is not believed to account for the observed asymmetries. It is probable that the anomalous behavior of these two patterns is due either to surface irregularities in the model itself or to asymmetric model mounting, or both. The surface irregularities could be geometrical deviations from an exact cone-sphere shape or may be imperfections in the conducting silver coat.

The same explanations probably apply to the asymmetric patterns obtained for measurements where a/λ was 6.09. In addition, for these measurements, the background levels were somewhat higher (5 to 10 db below the model return), and may also be contributing to the asymmetry. However, the patterns obtained at $a/\lambda = 0.60$ to 2.4 (Figs. 2 to 12) show a reasonable degree of symmetry. Apparently, the body-size-to-wavelength ratio is small enough that small surface perturbations on the model or slightly asymmetric mounting do not significantly affect the cross sections.

2. Average Nose-On Cross Section

Values of average measured cross section in the region ±45° from nose-on have been calculated and are given in Table II; these data are also plotted, along with those known average background levels vs frequency in Fig. 21, and a curve has been drawn to represent the trend which the data take. Where background was measured both before and after the model measurement, the highest of the two is plotted. In general, the exception being the measurements for $a/\lambda = 5.70$, the average background level is 4 db or more below the average measured cross section with the model present.

If it is assumed that there is no interaction between the background and the model, the true cross section of the model σ_t, at some aspect ψ, may be written as

$$\sigma_t = \sigma_m - \sigma_b - 2(\sigma_t \sigma_b)^{1/2} \cos \varphi \qquad (1)$$

where the measured cross section σ_m, the background return σ_b, and the phase difference φ between the background and model returns are all functions of ψ. Thus, depending on the background level and its phase relative to the model return, the desired true cross section can be less than, equal to, or greater than the measured cross section. For the measurements reported herein, no phase data are available; thus, we can only indicate the limits on the true cross section as a function of background return. This is done in Fig. 22; both quantities are plotted in decibels relative to the measured model return.

When considering the average true cross section over some range of aspect angles, the terms in Eq. (1) become average quantities, i.e.,

$$\overline{\sigma}_t = \overline{\sigma}_m - \overline{\sigma}_b - \overline{2(\sigma_t \sigma_b)^{1/2} \cos \varphi} \qquad (2)$$

where the bars indicate averages taken over the region of interest. As noted above, $\bar{\sigma}_b$ was in general 4 db or more below $\bar{\sigma}_m$. However, estimates of the term $2(\sigma_t\sigma_b)^{1/2}\cos\varphi$ are not easily made, and all one can say definitely is that the average cross-section values given in Table II fall within the limits indicated in Fig. 22 for the worst ratio σ_b/σ_m observed in the region of interest.

3. Comparison of Direct Nose-On Scattering with Theory

It is generally considered that the nose-on backscatter from a cone-sphere arises from three sources; viz., tip scattering, traveling waves, and creeping waves.* (See Fig. 23.) The magnitudes and phases of these components may be roughly determined theoretically, and may then be combined to provide a theoretical estimate of the nose-on backscatter from a cone-sphere. Thus, we have

$$\frac{\sigma}{\lambda^2} = \frac{1}{\pi}\left|S_1 \exp[i\varphi_1] + S_2 \exp[i\varphi_2] + S_3 \exp[i\varphi_3]\right|^2 \tag{3}$$

where

σ is the nose-on backscatter cross section of the cone-sphere,

S_j is the amplitude of the j^{th} scattering component,

φ_j is the phase of the j^{th} scattering component,

where

1 refers to tip scatter,

2 refers to the traveling wave,

3 refers to the creeping wave.

The first component, attributed to the tip, is the only backscattering component theoretically predicted to occur for a cone of infinite length. The physical optics solutions for both the infinite cone and the cone-sphere indicate that the tip scattering component, nose-on, is[3,5]

$$S_1 \exp[i\varphi_1] = \frac{-i}{4}\tan^2\alpha \exp[4\pi i(a/\lambda)\csc\alpha] \tag{4}$$

where α is the cone half angle and a is the radius of the sphere. For conditions of interest here, $\alpha = 12.5°$, and Eq. (4) then gives for the cross section

$$\frac{\sigma_1}{\lambda^2} = 4.8 \times 10^{-5} \quad .$$

Hence, the cross section from tip scattering is 43 db below λ^2, and this is small enough that it may generally be neglected.

The second component is believed to result from waves which travel along the cone surface and are scattered upon reaching the discontinuity in curvature at the junction of the cone and sphere surfaces. By physical optics methods,[3] it may be shown that

$$S_2 \exp[i\varphi_2] = \frac{i}{4}\sec^2\alpha \exp[4\pi i(a/\lambda)\sin\alpha] \quad . \tag{5}$$

* See Ref. 3, and also Refs. 2 and 4.

TABLE III

COMPARISON OF NOSE-ON DATA WITH THEORY

		Nose-On Cross Section		Values of Cross Section in Nose-On Region			
				Maximum	Minimum	Maximum	Minimum
a/λ	Polarization	Measured ($db\lambda^2$)	Predicted ($db\lambda^2$)	Measured ($db\lambda^2$)	Measured ($db\lambda^2$)	Predicted ($db\lambda^2$)	Predicted ($db\lambda^2$)
0.60	HH	−16	−12	−8	−23	−8	−20
	VV	−14		−11	−15		
1.45	HH	−12	−10	−11	−27	−9	−24
	VV	−14		−10	−24		
1.47	HH	−10	−9	−10	−23	−9	−24
	HH	−10		−7	−15		
	VV	−10		−9	−13		
1.57	HH	−6	−12	−6	−23	−9	−25
	VV	−10		−9	−20		
2.40	HH	−5	−14	−5	−27	−10	−36
	VV	−6		−5			
3.91	HH	−12	−14	−12	−28	−12	−29
	VV	−12		−7	−27		
5.70	HH	−11	−15	−8	−17	−13	−23
	VV	−16		−8	−16		
6.09	HH	−11	−14	−12	−21	−13	−22
	VV	−9		−9	−22		
10.43	HH	−11	−15	+5	−20	−15	−20
	VV	−10		+1	−25		

The third component is attributed to creeping waves which travel around the shadow, or rear, portion of the cone-sphere. Such creeping waves also contribute to scattering by a conducting sphere. In fact, the cross section of a sphere may be written as the sum of two terms[6]

$$\frac{\sigma_s}{\lambda^2} = \frac{1}{\pi} \left| S_g \exp[i\varphi_g] + S_3 \exp[i\varphi_3] \right|^2 = \frac{1}{\pi} \left| S_s \exp[i\varphi_s] \right|^2 \qquad (6)$$

where S_g and φ_g refer to the geometric optics contribution and σ_s, S_s, and φ_s are the values rigorously derived for a sphere.

By inverting Eq. (6) the creeping wave component may be found from a knowledge of S_s, φ_s, S_g, and φ_g. It may be shown that

$$S_g \exp[i\varphi_g] = -\frac{1}{2} i \left[\frac{2\pi a}{\lambda} + \frac{1}{2} i\right] \exp[4\pi i(a/\lambda)]$$

and tables of S_s and φ_s obtained by the method of Mie are available.[7,8] In this way, all the quantities in Eq. (1) may be found and the desired cross section σ calculated. The results of these theoretical calculations are compared with the measured cross sections in Table III. The nose-on cross section should be the same for both polarizations, so only one calculated value is indicated.

In addition, Figs. 24 and 25 give a comparison between the nose-on cross section, as calculated above, and a relatively large set of experimental results, replotted from Ref. 3, obtained by Blore and Royer[9] and by Moffatt.[2,4] Figure 26 presents the theoretical cross section for a cone-sphere with $\alpha = 15°$ for sphere radii of up to ten wavelengths. Also indicated on Fig. 26 is the contribution σ_j of each component to the resulting cross section.

It may be seen that the agreement between the theoretical and the measured cross sections is reasonable for the smaller values of a/λ, and that the deviations appear to increase as a/λ increases, when the relative contribution of the traveling wave component becomes larger. It is thereby inferred that the physical optics value for this component, as given by Eq. (5), is too small. As yet, experimental measurements do not provide a sufficiently reliable basis to determine whether or not this is so.

In the nose-on region, for aspect angles roughly between $\pm\alpha°$, it is expected that the magnitude of each of the three scattering components remains approximately constant, and that oscillations in the cross section appear which are due to interference between these components. Therefore, we should be able to predict the maxima, and to a lesser degree of accuracy, the minima, of the backscatter in this region. In Table III, the predicted maxima and minima are compared with the experimental results. The equations employed were

$$\frac{\sigma}{\lambda^2} = \frac{1}{\pi} \left(|S_1| + |S_2| + |S_3| \right)^2$$

for the maxima, and

$$\frac{\sigma}{\lambda^2} = \frac{1}{\pi} \text{ times the maximum of } \left\{ \begin{array}{l} \left(|S_2| - |S_3| \right)^2 \\ |S_1|^2 \end{array} \right\}$$

for the minima.

B. Cone Specular Reflection

At aspect angles of ±77.5°, large lobes caused by specular reflection from the conical surface of the model appear in the scattering patterns. The measured values of cross section and lobe width are tabulated in Table II and plotted in Figs. 27 and 28. The theoretical values shown were calculated by approximating the conical section by an "equivalent cylinder" and calculating the specular return for this body. The "equivalent cylinder" is defined as that cylinder whose length is the length of the conical surface and whose radius is such that the volume of the cylinder is equal to that of the cone. The physical optics approximation to the specular return from a cylinder is[5]

$$\sigma = \frac{2\pi a L^2}{\lambda}$$

where a is the cylinder radius, L is the length, and λ is the wavelength of the incident wave. One may predict the width $\Delta\Theta$ of the specular lobe by

$$\Delta\Theta = \frac{\lambda}{L} \quad .$$

It may be seen, in Figs. 27 and 28, that the measured data are in reasonable agreement with the theoretical curves.

C. Sphere Specular Reflection

At aspect angles from 90° to 270°, the dominant contribution to the backscattering cross section is the specular return from the spherical cap. Values of average cross section in the 90° to 270° region were calculated from the measured data and are given in Table II and plotted in Fig. 29. The theoretical curve shown is the geometric optics value given by

$$\frac{\sigma}{\lambda^2} = \pi\left(\frac{a}{\lambda}\right)^2 \quad .$$

The measured values bracket the theoretical value, the greatest deviation being about 2 db.

REFERENCES

1. J. Rheinstein, "Scattering of Electromagnetic Waves by an Eaton Lens," Technical Report 273 [U], Lincoln Laboratory, M. I. T. (28 June 1962), DDC 289380.
2. D. L. Moffatt, "Low Radar Cross-Sections, The Cone-Sphere," Ohio State University Research Foundation, Report No. 1223-5 (15 May 1962).
3. R. E. Kleinman, et al., "Studies in Radar Cross Sections XLVIII – Scattering and Diffraction by Regular Bodies – II: The Cone," University of Michigan, Radiation Laboratory, Scientific Report No. 5 (January 1963).
4. E. M. Kennaugh, et al., "On the Axial Echo Area of the Cone-Sphere Shape," Proc. IRE 50, 199 (1962).
5. J. R. Mentzer, Scattering and Diffraction of Radio Waves (Pergamon Press, New York, 1955), p. 108.
6. H. C. Van de Hulst, Light Scattering by Small Particles (Wiley, New York, 1957), p. 372.
7. M. E. Bechtel, "Scattering Coefficients for the Backscatter of Electromagnetic Waves from Perfectly Conducting Spheres," Cornell Aeronautical Laboratory, Report No. AP/RIS-1 (December 1962).
8. J. Rheinstein, "Tables of the Amplitude and Phase of the Backscatter from a Conducting Sphere," G-Report 22G-16 [U], Lincoln Laboratory, M. I. T. (19 June 1963), DDC 409820, H-522.
9. W. E. Blore, "Experimental Measurements of the Radar Cross Section of a Cone Sphere," Proc. IEEE 51, 1263 (1963).

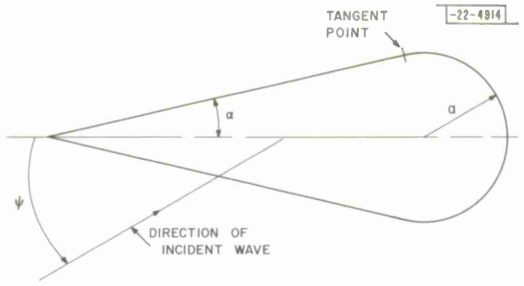

Fig. 1. Measurement geometry.

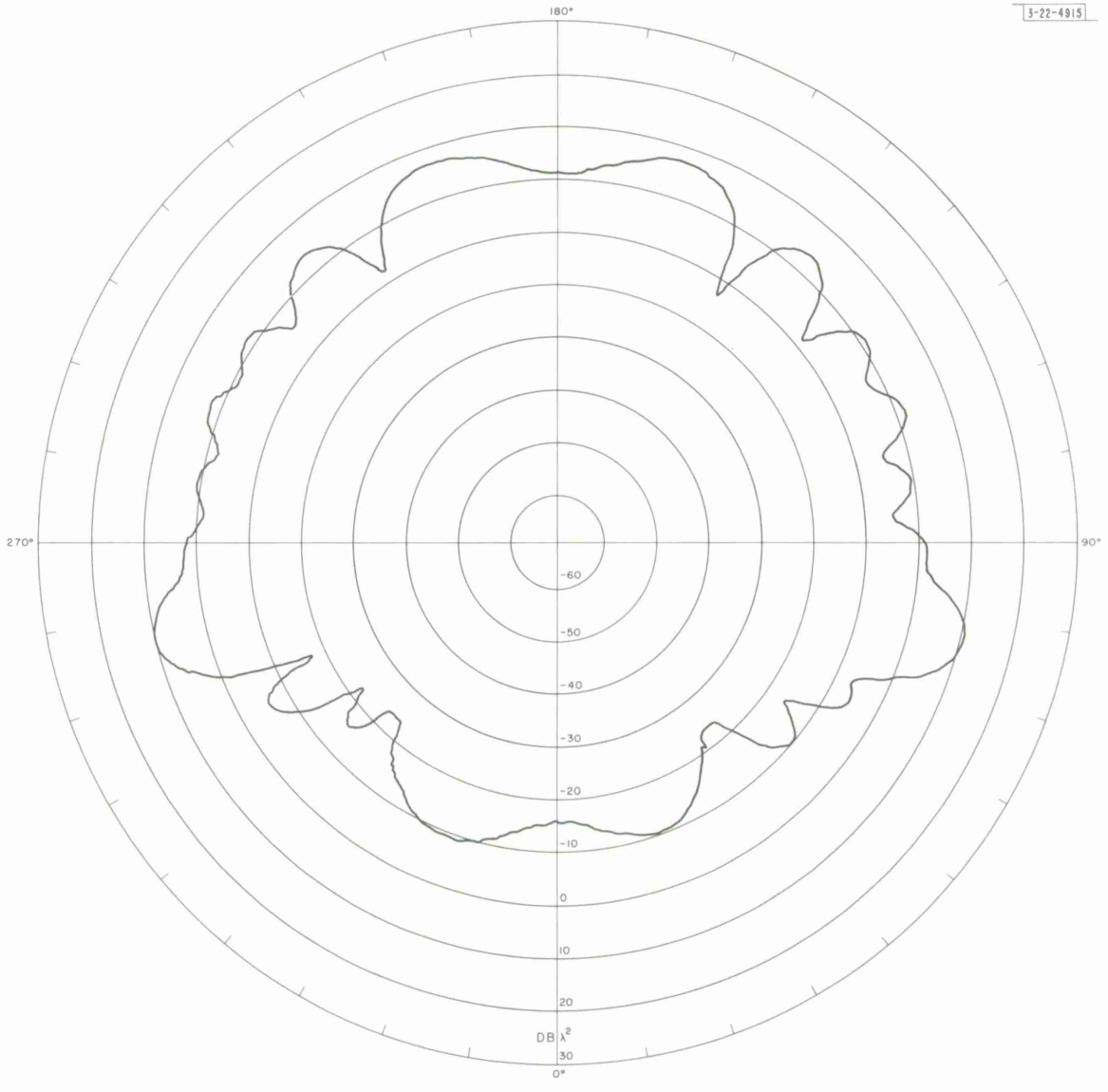

Fig. 2. Backscatter cross section, $a/\lambda = 0.60$ HH polarization.

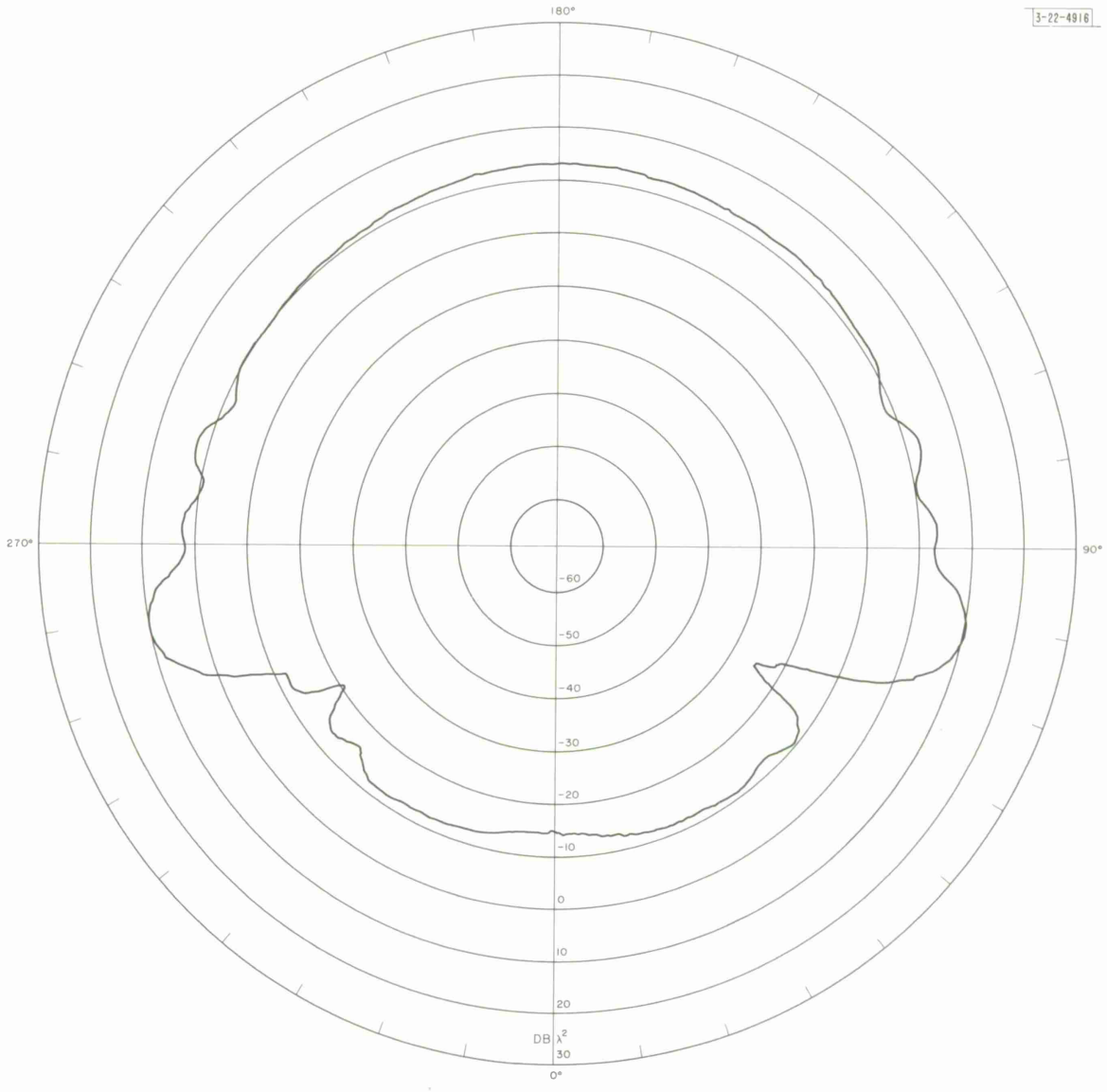

Fig. 3. Backscatter cross section, $a/\lambda = 0.60$ VV polarization.

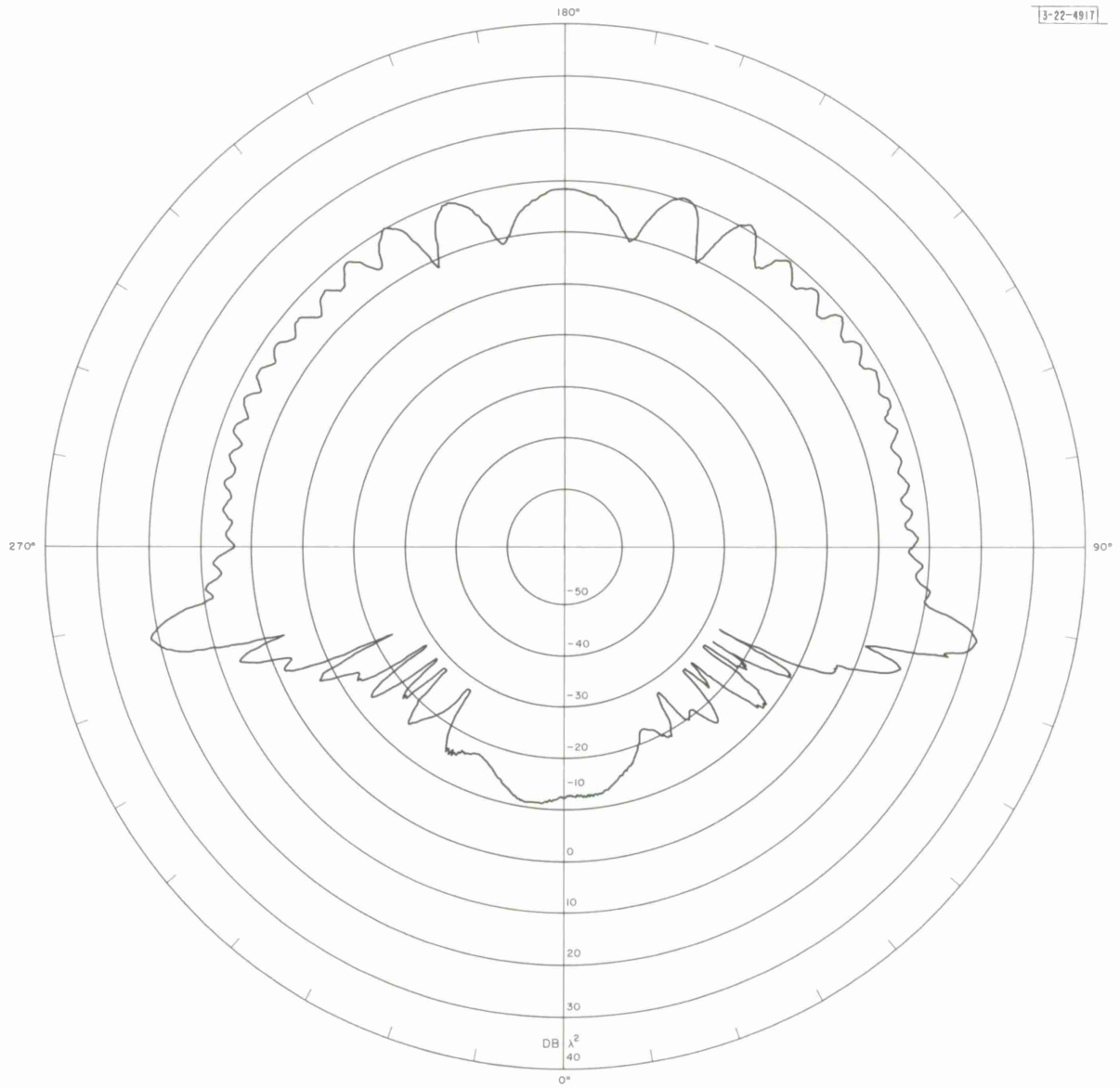

Fig. 4. Backscatter cross section, $a/\lambda = 1.45$ HH polarization.

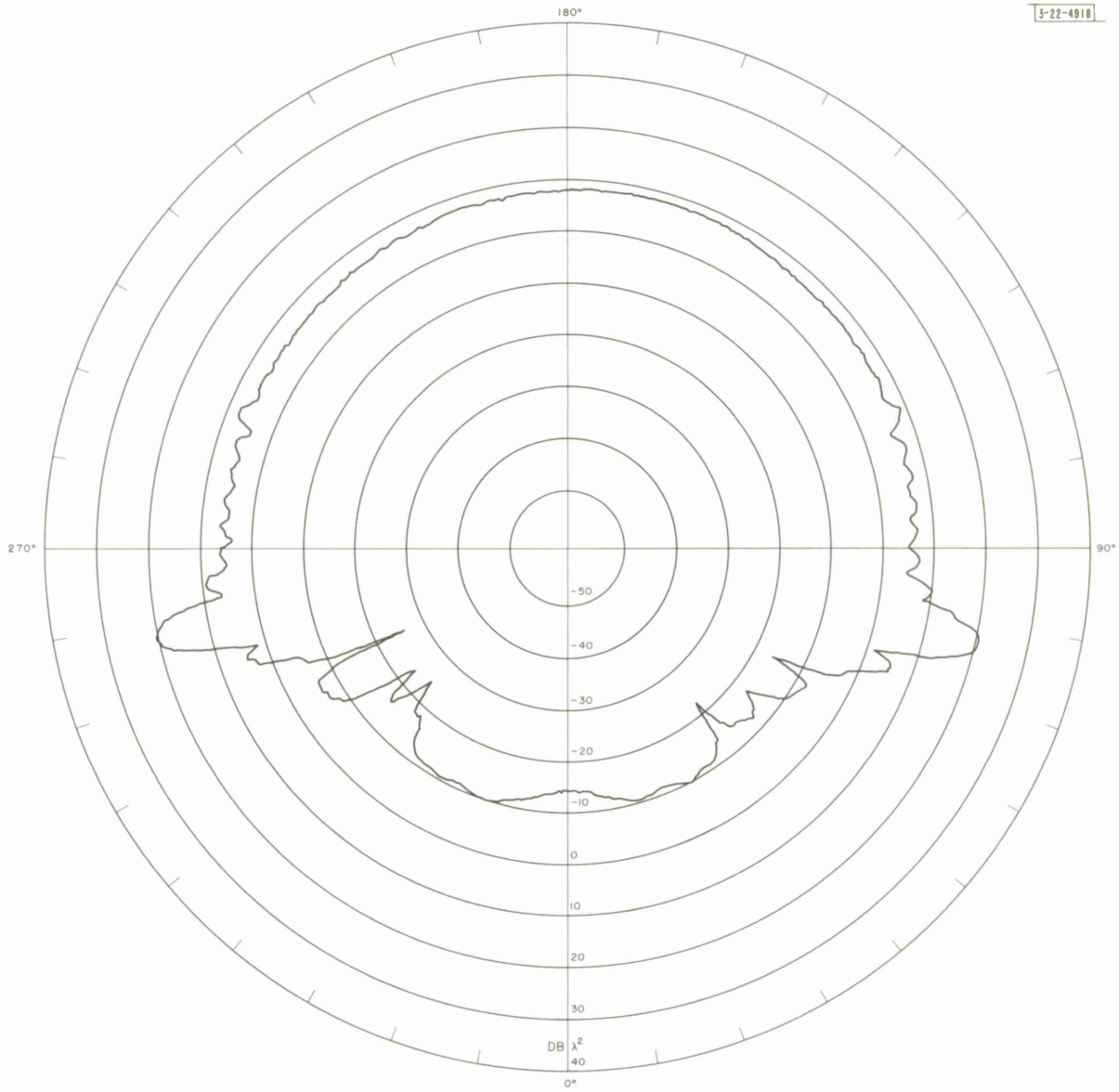

Fig. 5. Backscatter cross section, $a/\lambda = 1.45$ VV polarization.

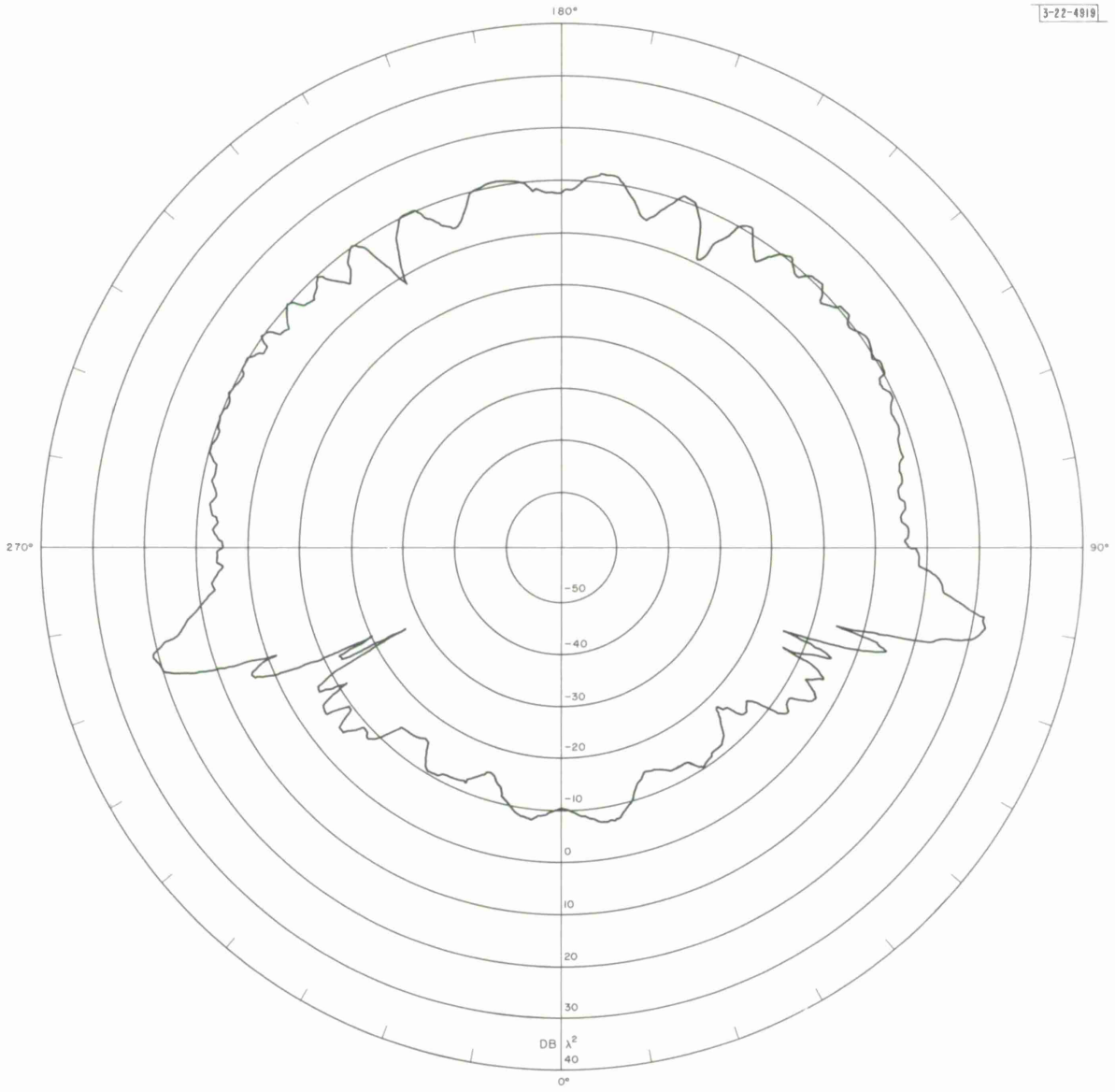

Fig. 6. Backscatter cross section, $a/\lambda = 1.47$ HH polarization $[d = 2.4(D^2/\lambda)]$.

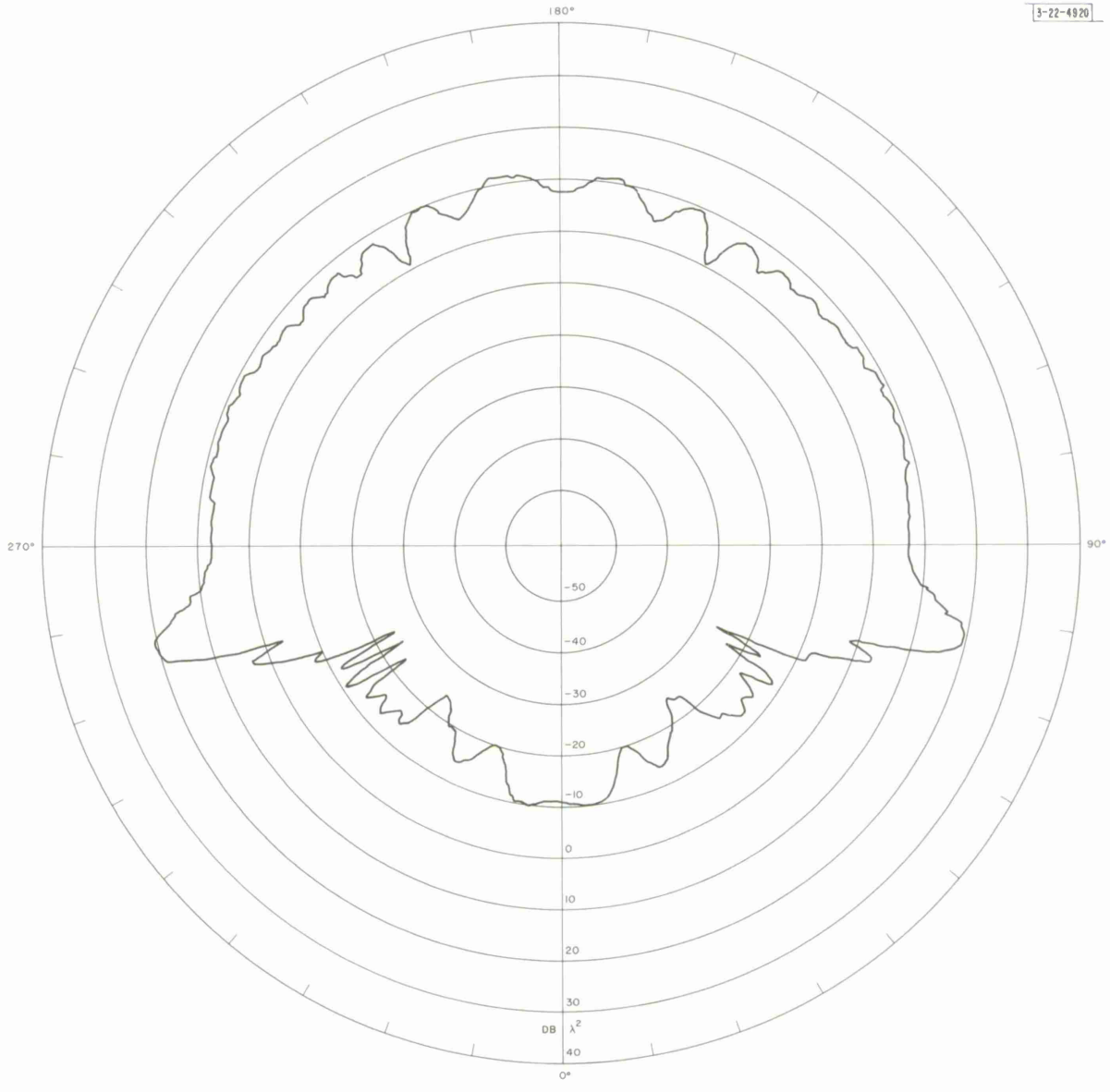

Fig. 7. Backscatter cross section, $a/\lambda = 1.47$ HH polarization $[d = 1.5(D^2/\lambda)]$.

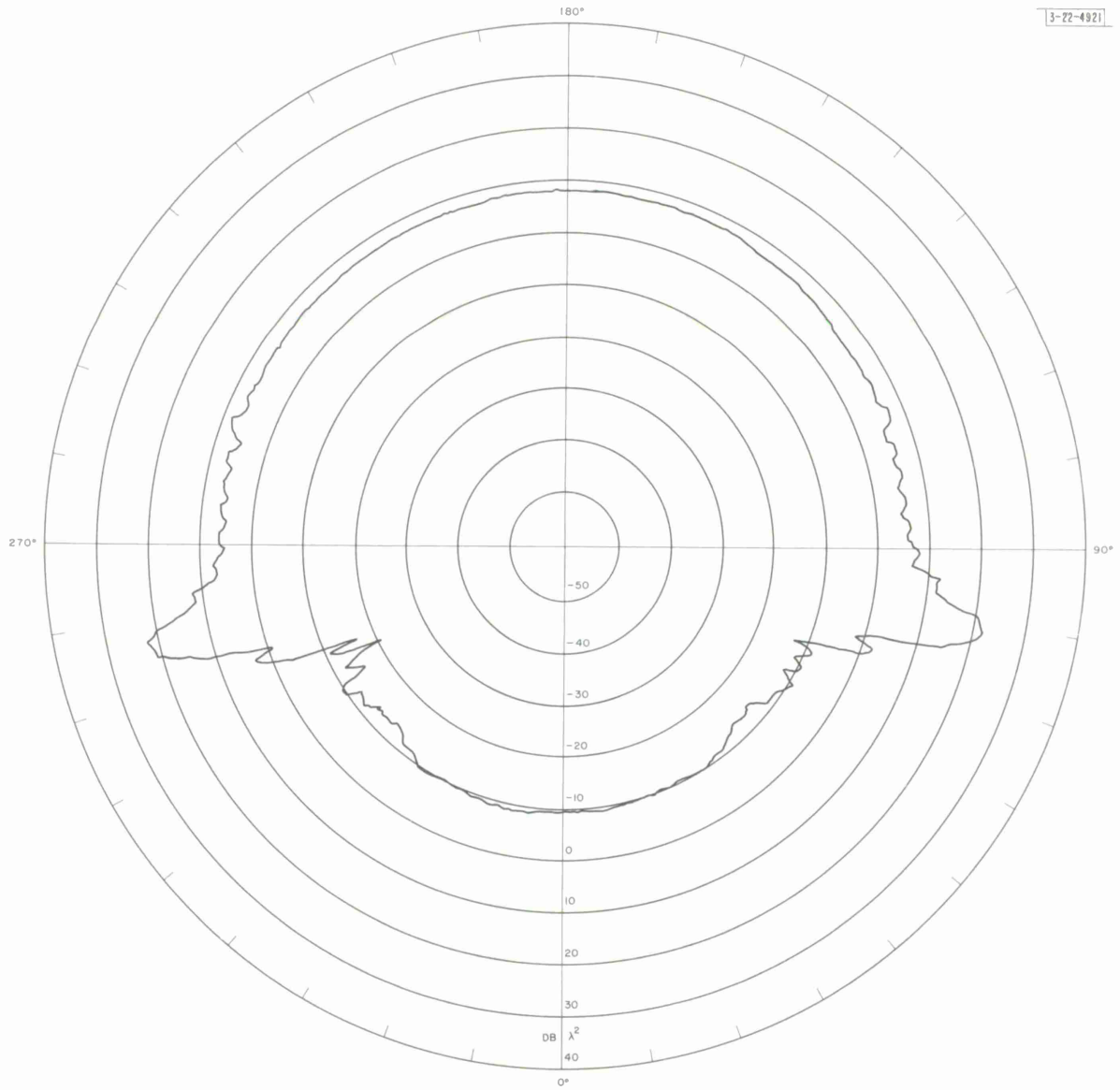

Fig. 8. Backscatter cross section, $a/\lambda = 1.47$ VV polarization.

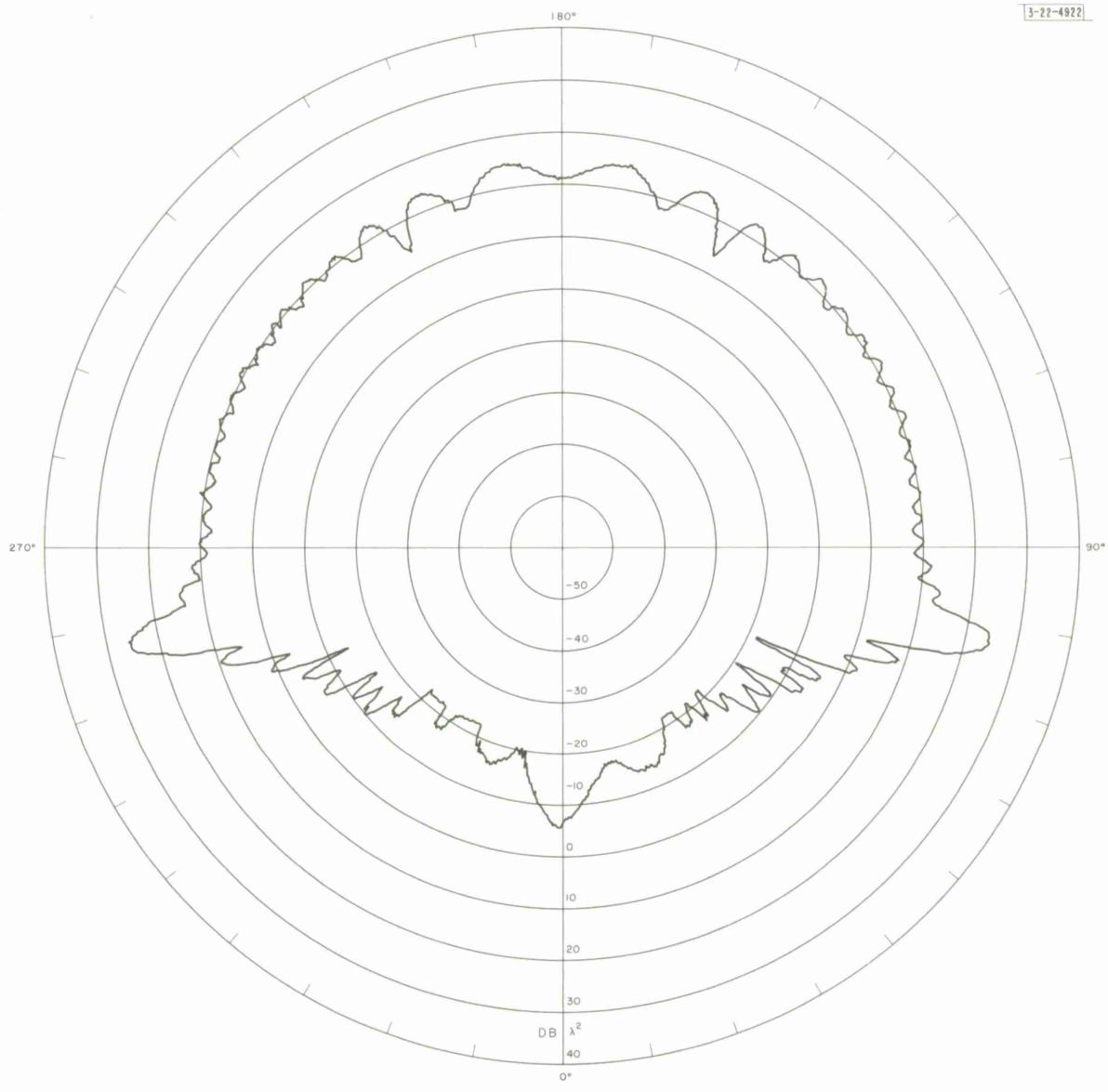

Fig. 9. Backscatter cross section, $a/\lambda = 1.57$ HH polarization.

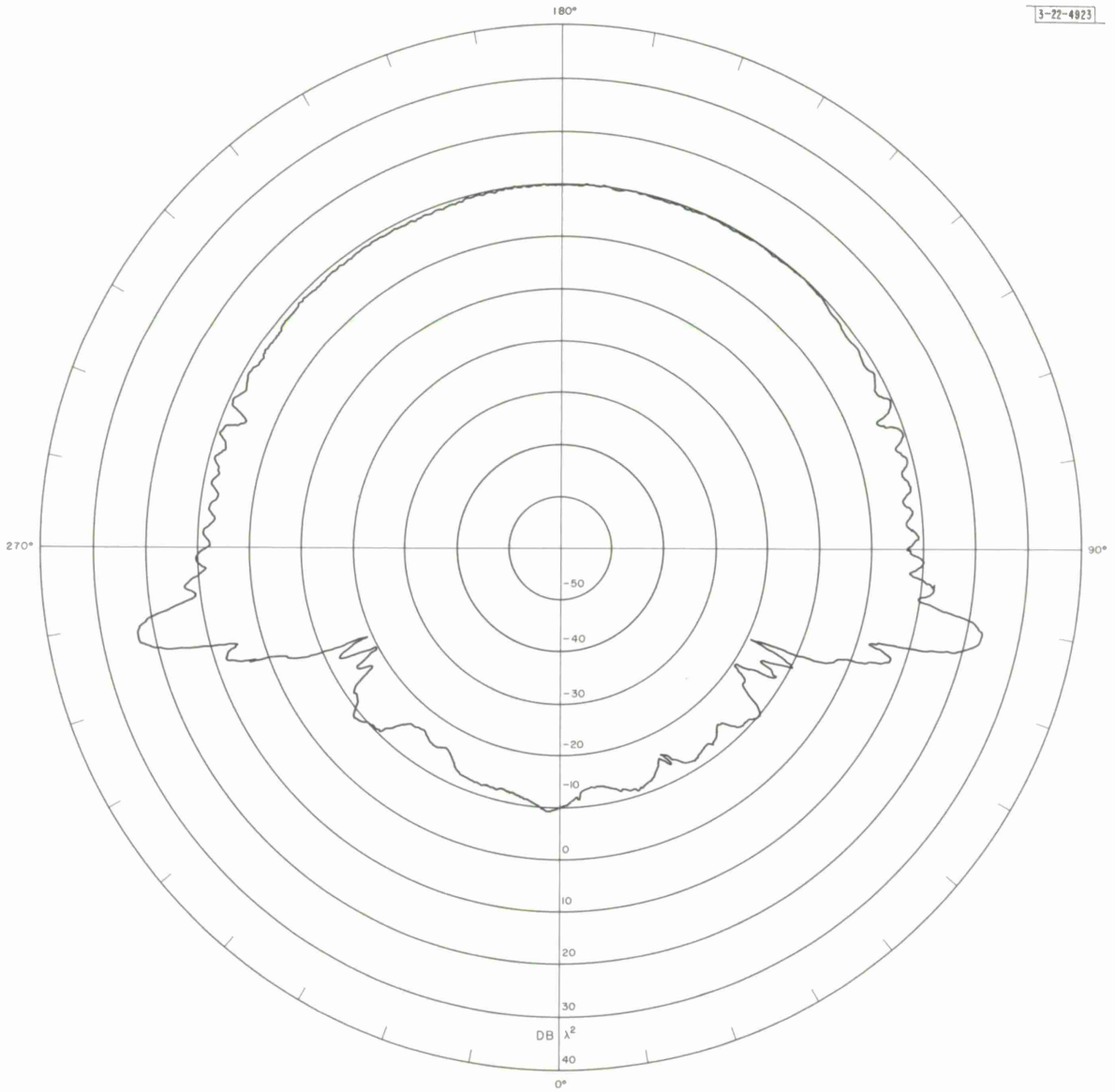

Fig. 10. Backscatter cross section, $a/\lambda = 1.57$ VV polarization.

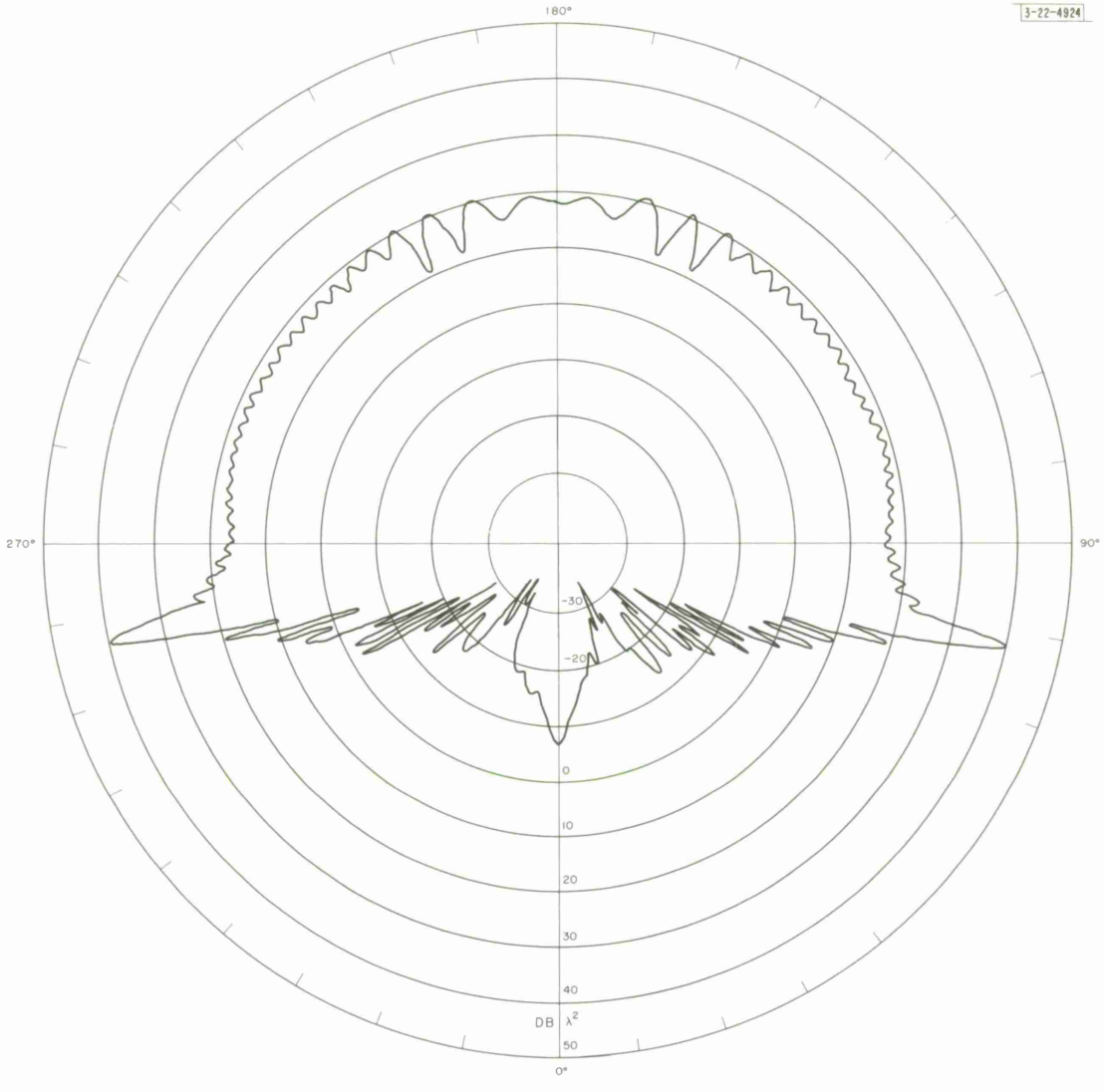

Fig. 11. Backscatter cross section, $a/\lambda = 2.4$ HH polarization.

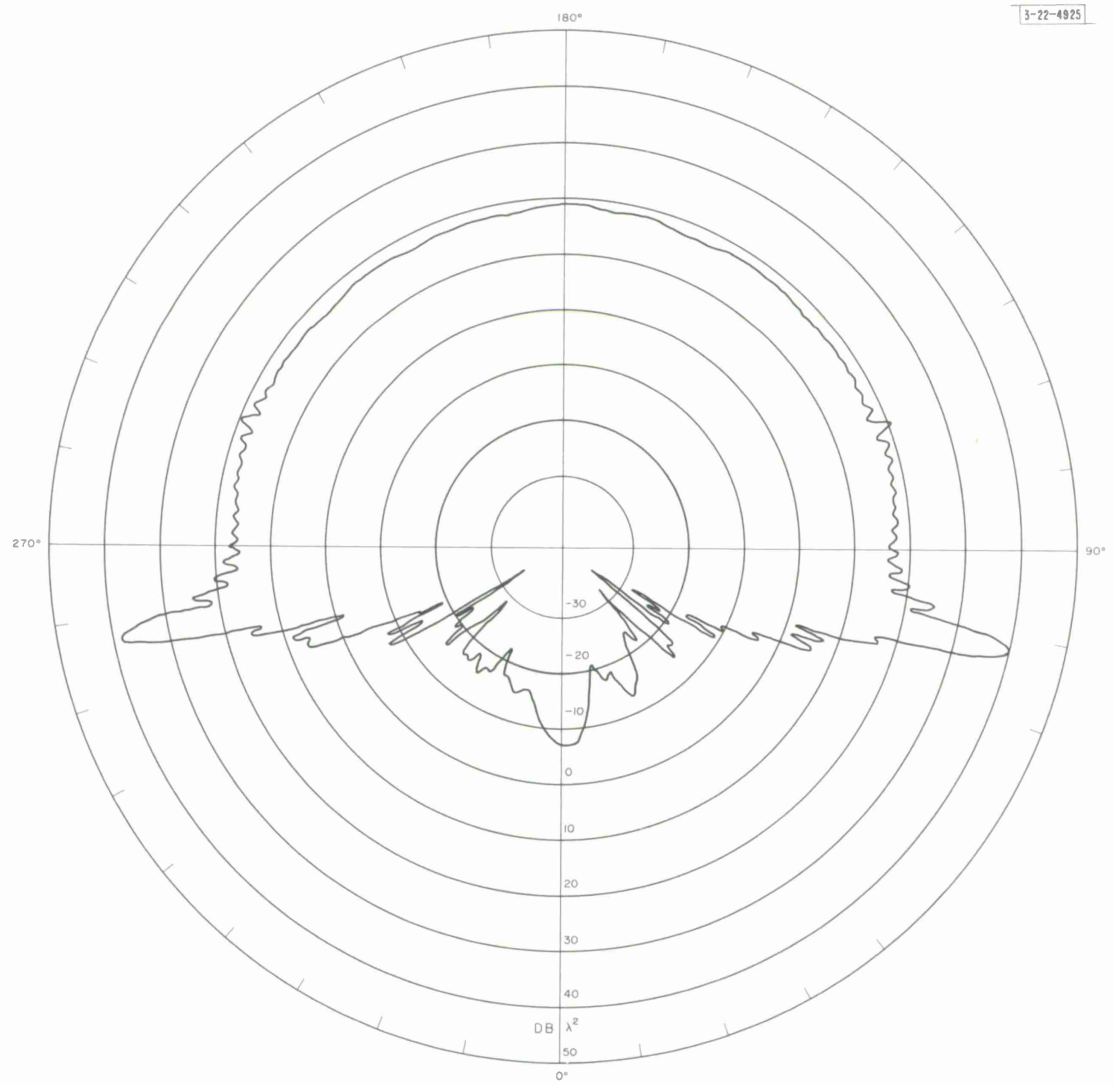

Fig. 12. Backscatter cross section, $a/\lambda = 2.4$ VV polarization.

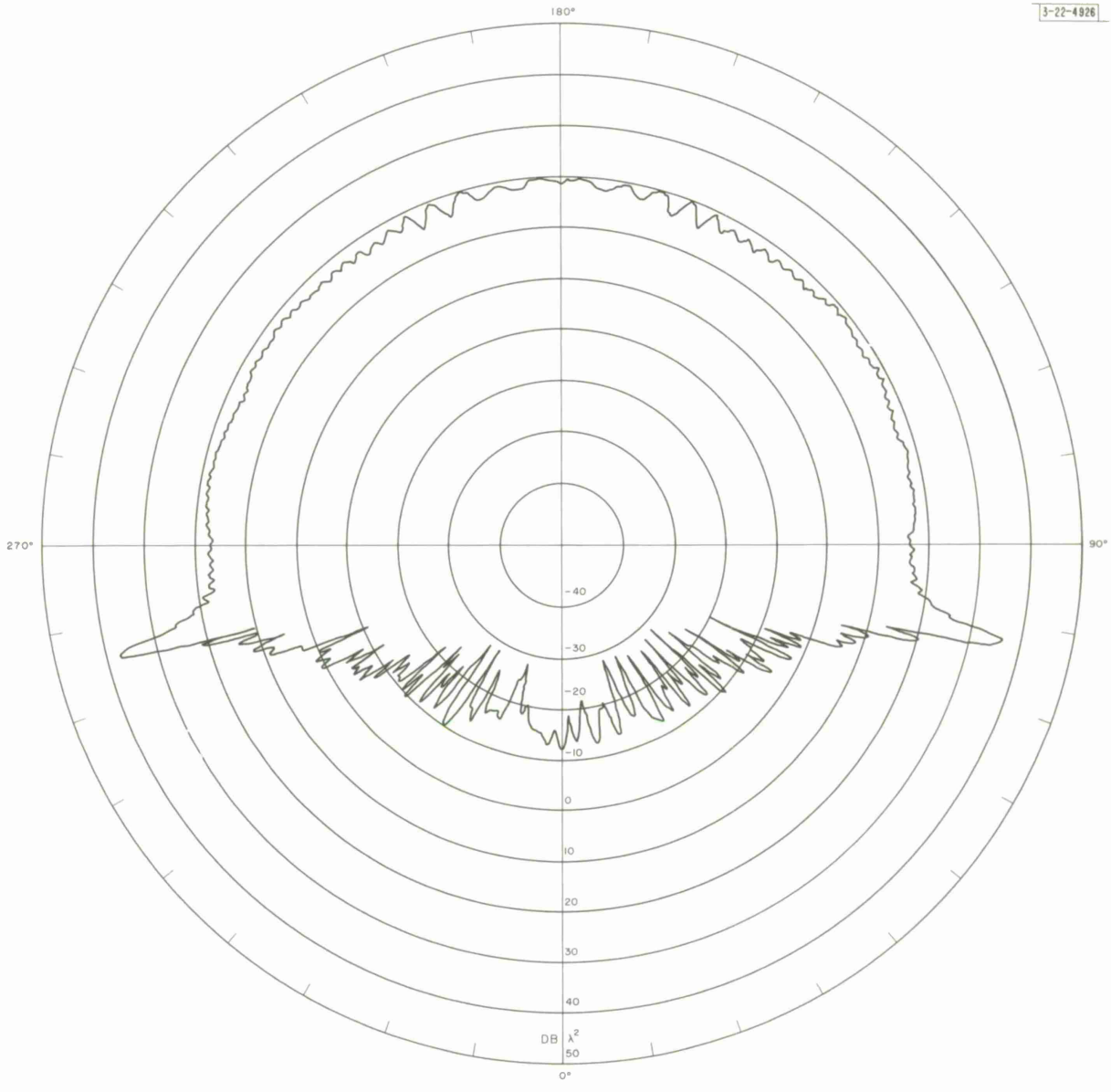

Fig. 13. Backscatter cross section, $a/\lambda = 3.91$ HH polarization.

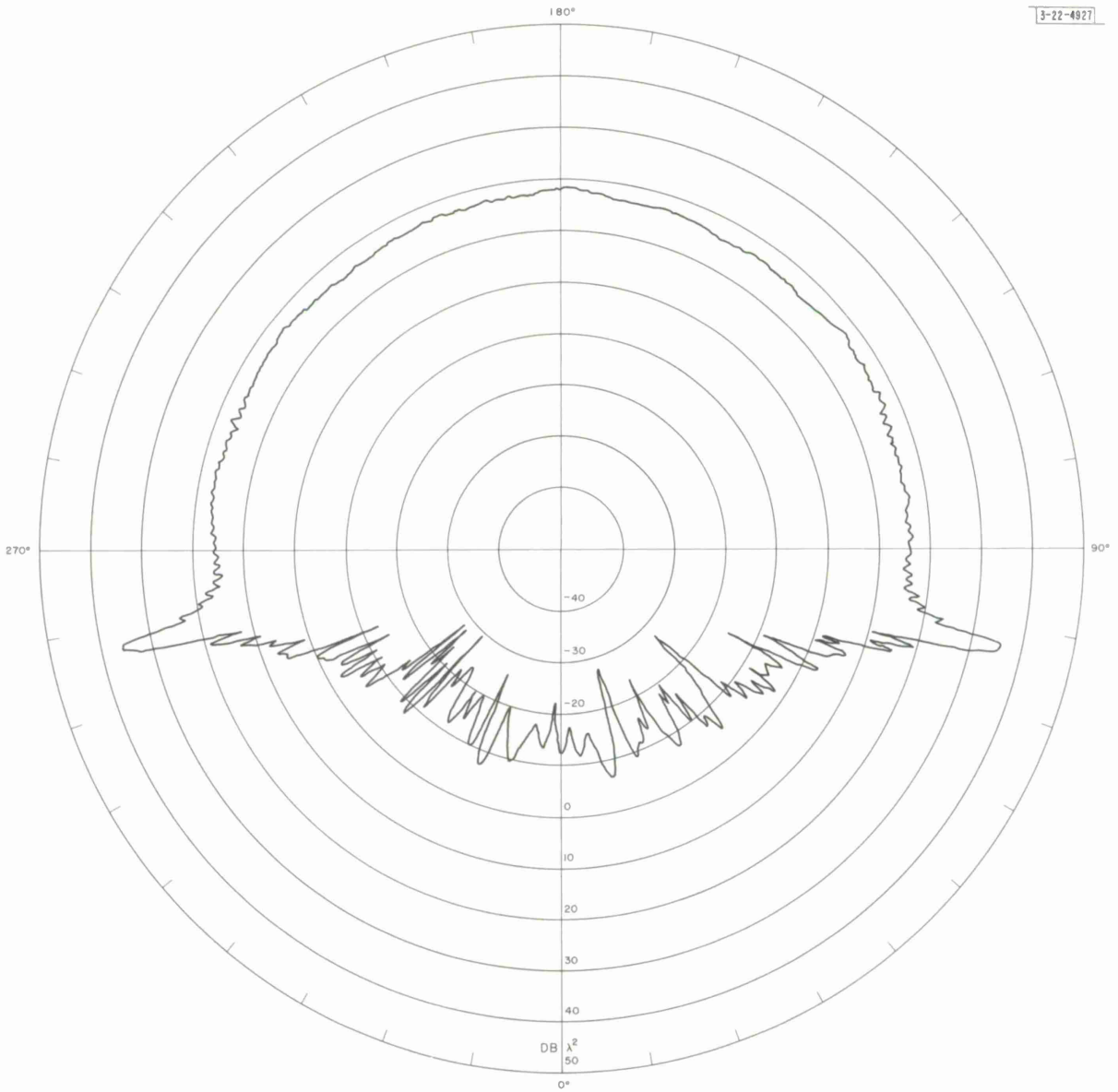

Fig. 14. Backscatter cross section, $a/\lambda = 3.91$ VV polarization.

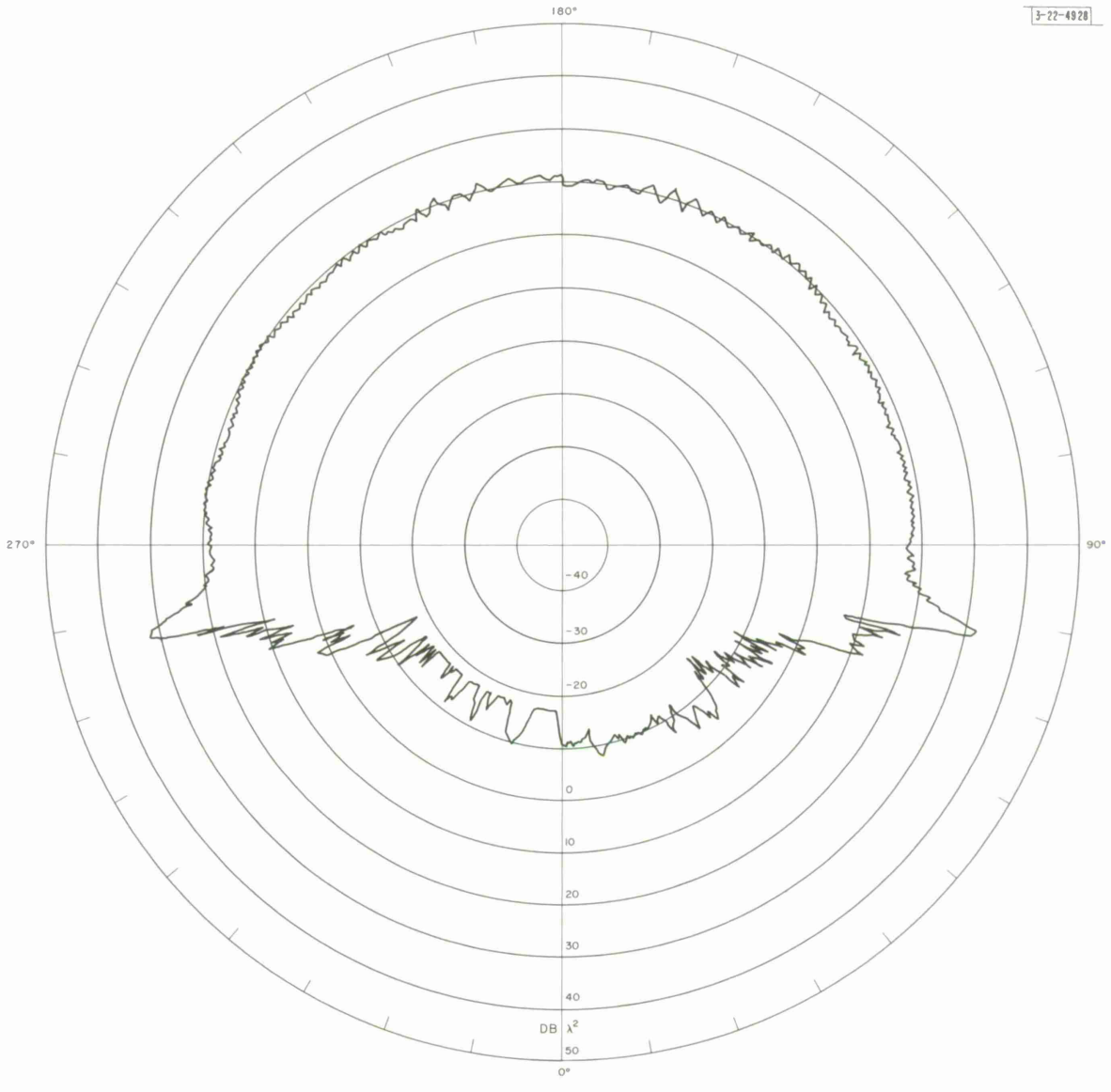

Fig. 15. Backscatter cross section, $a/\lambda = 5.70$ HH polarization.

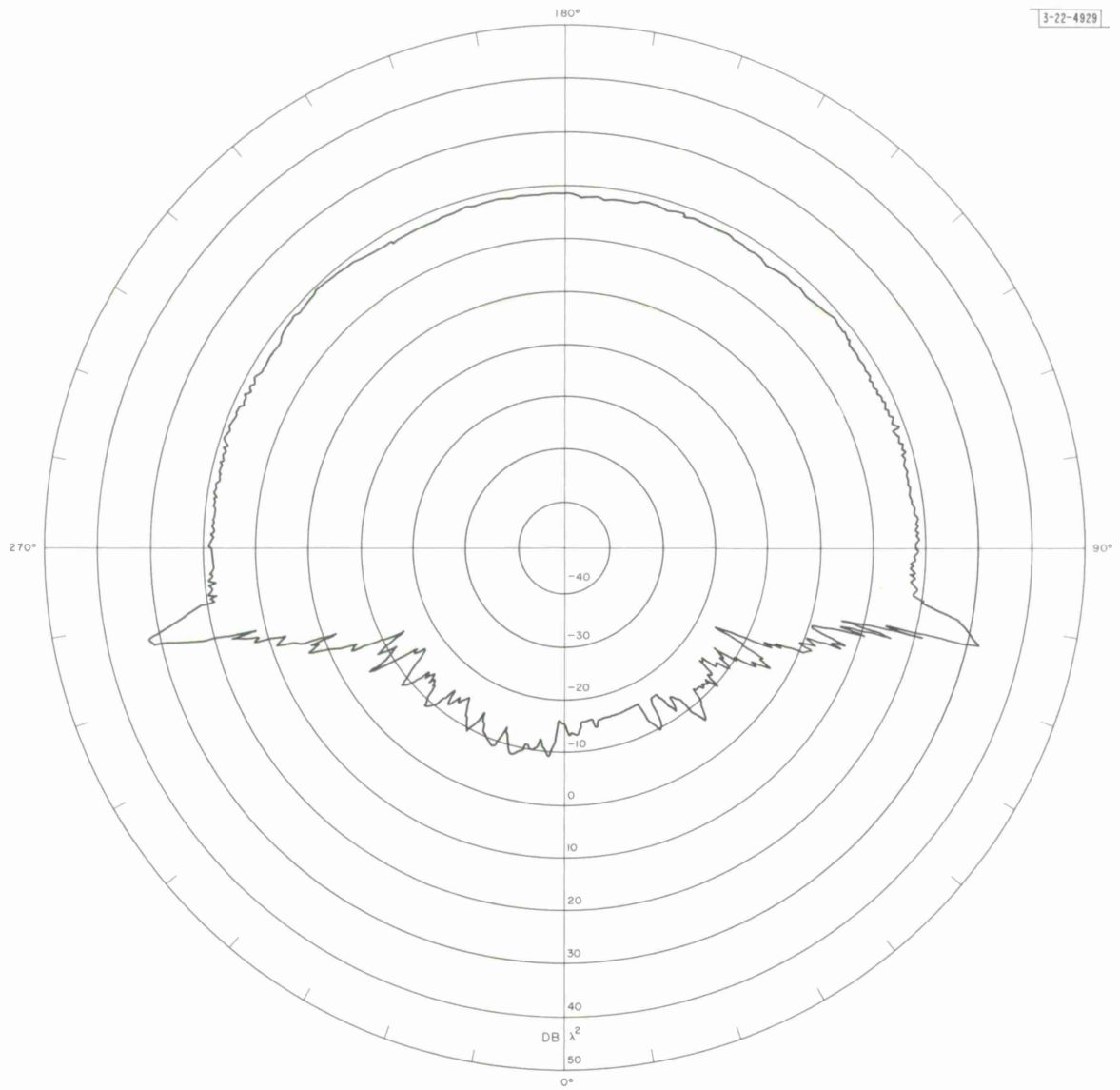

Fig. 16. Backscatter cross section, $a/\lambda = 5.70$ VV polarization.

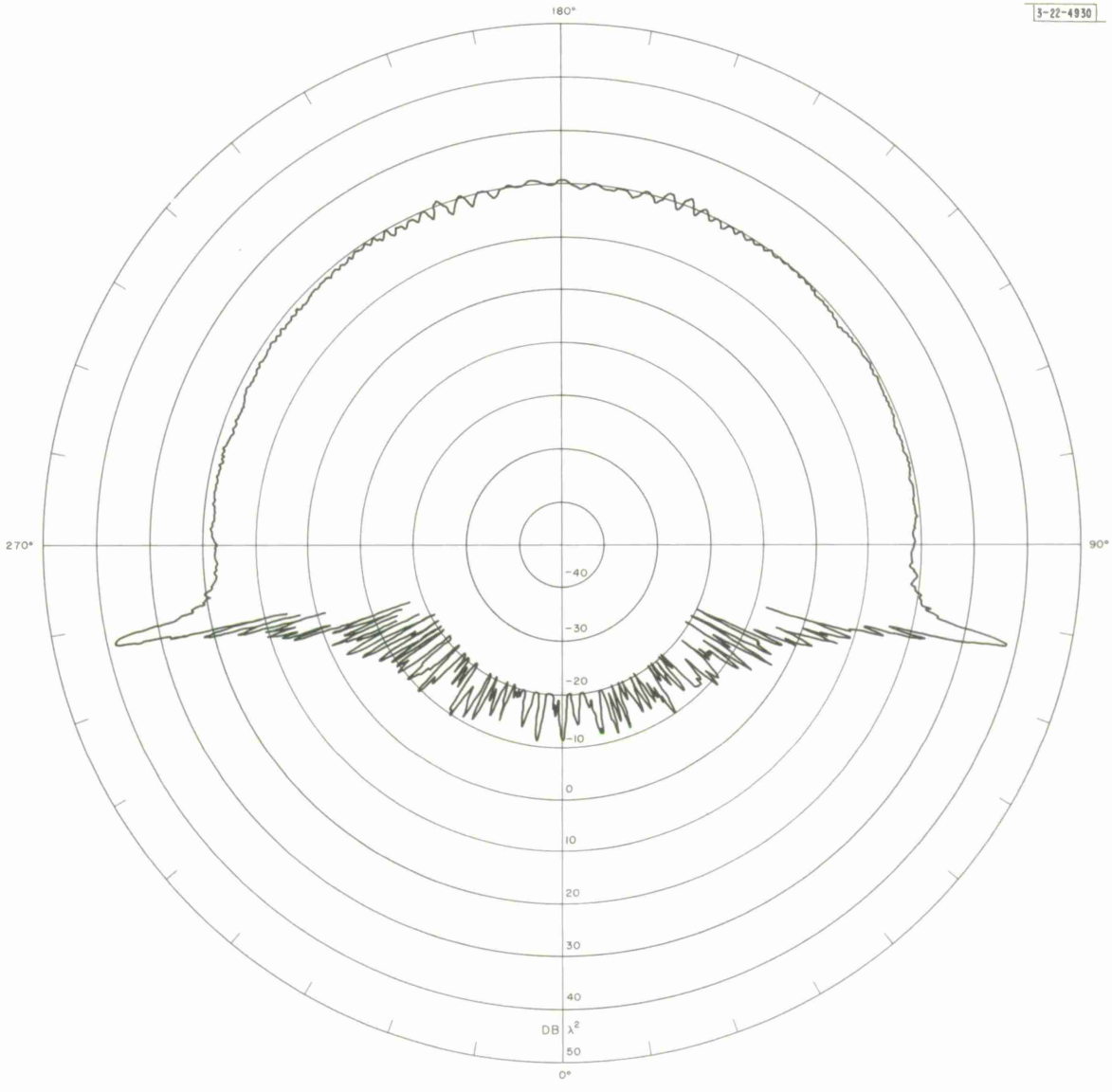

Fig. 17. Backscatter cross section, $a/\lambda = 6.09$ HH polarization.

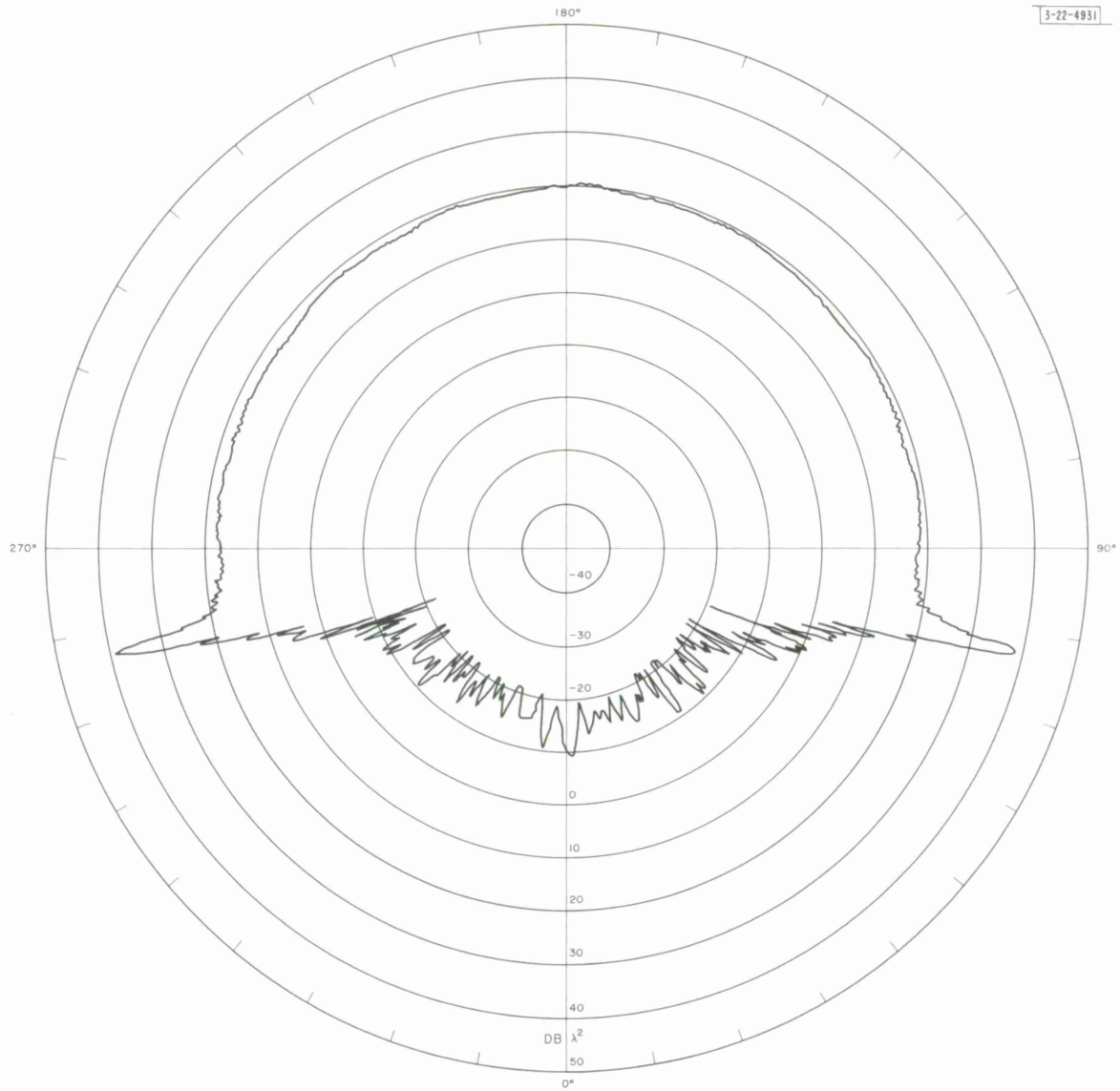

Fig. 18. Backscatter cross section, $a/\lambda = 6.09$ VV polarization.

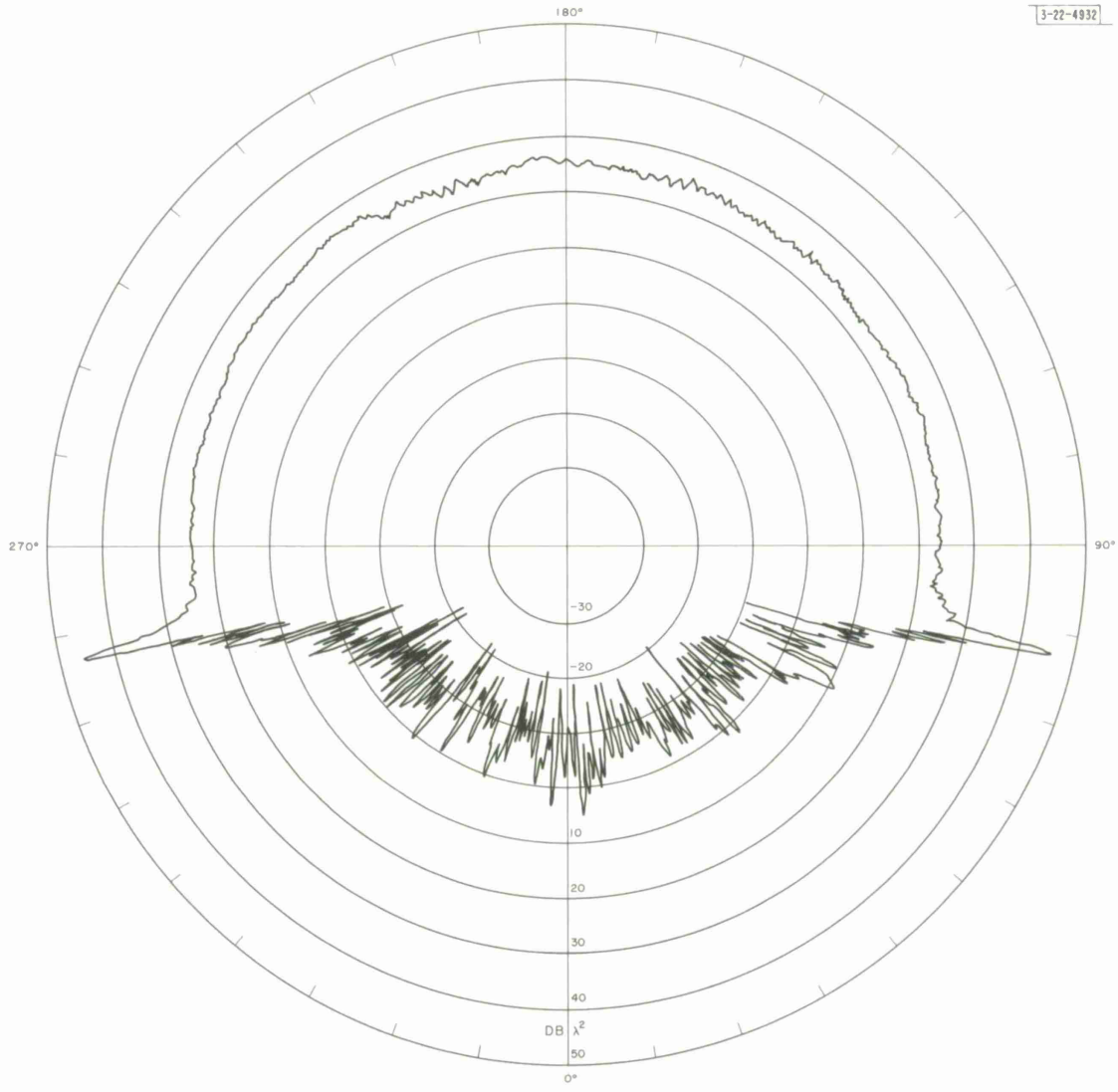

Fig. 19. Backscatter cross section, $a/\lambda = 10.4$ HH polarization.

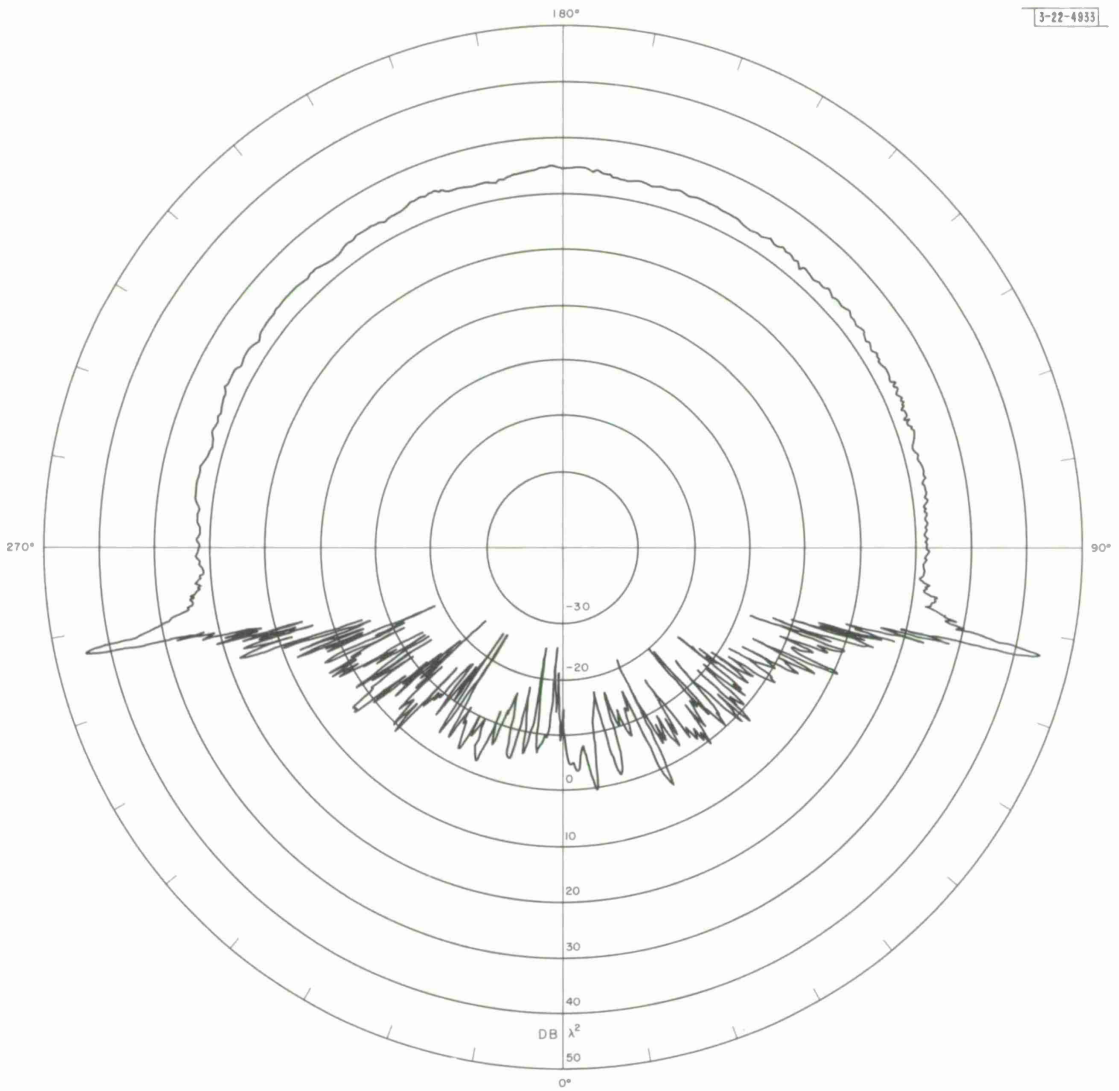

Fig. 20. Backscatter cross section, $a/\lambda = 10.4$ VV polarization.

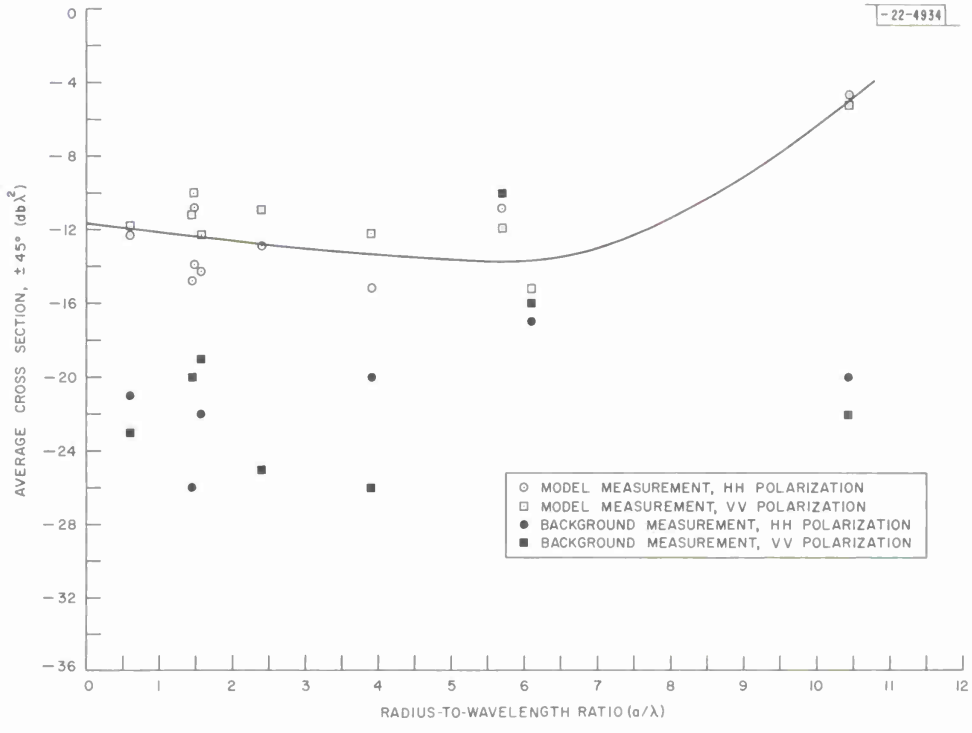

Fig. 21. Average nose-on cross section vs radius-to-wavelength ratio.

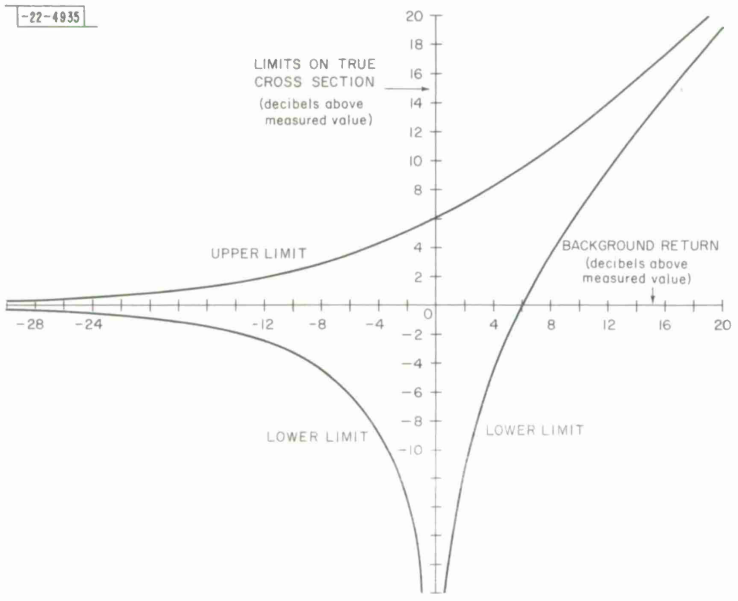

Fig. 22. Limits on true cross section vs background return.

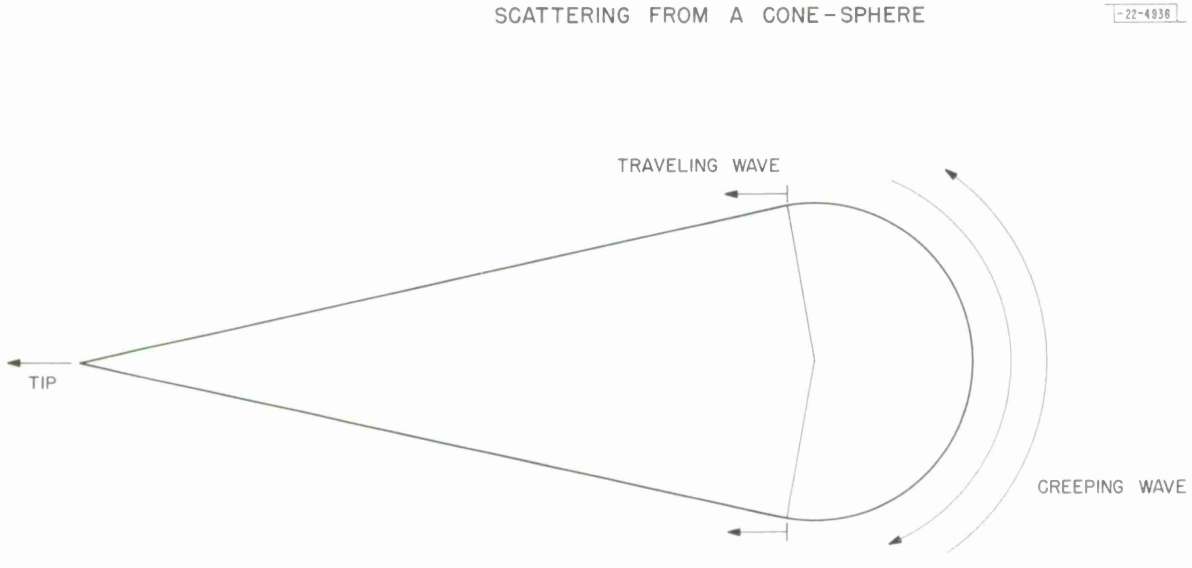

Fig. 23. Scattering sources.

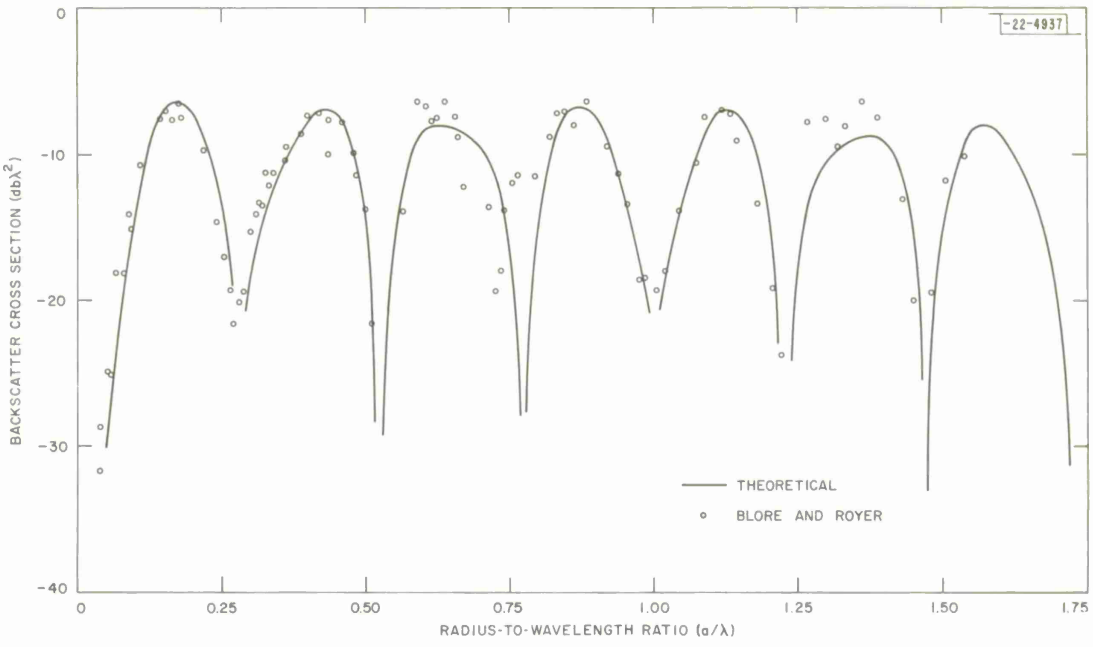

Fig. 24. Comparison between predicted and measured nose-on backscatter cross sections of a 30° half-angle cone-sphere.

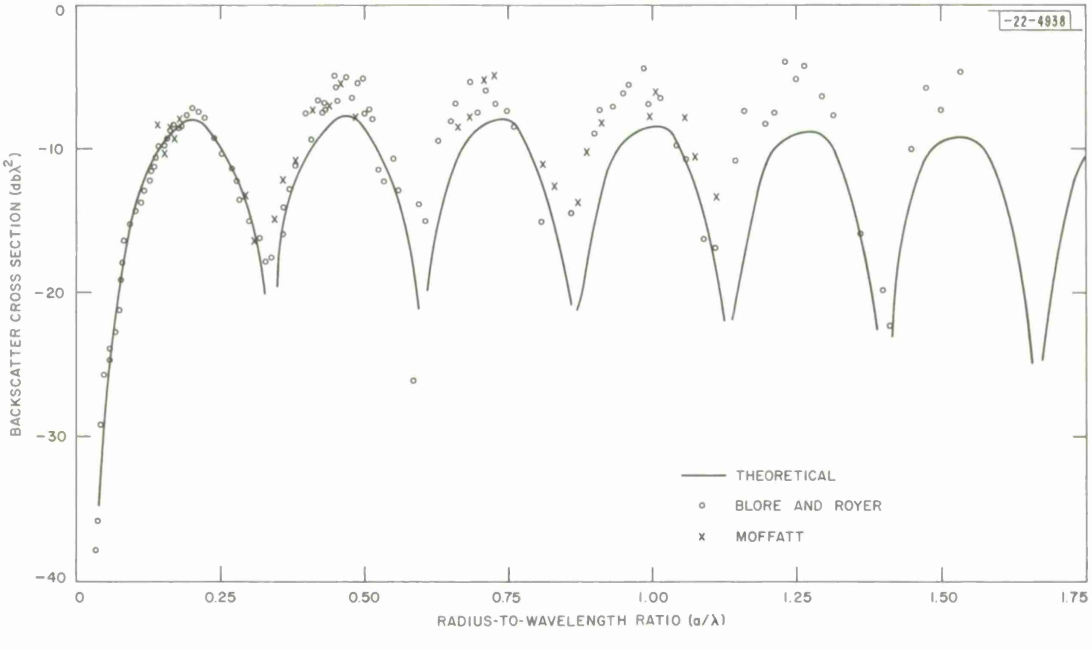

Fig. 25. Comparison between predicted and measured nose-on backscatter cross sections of a 15° half-angle cone-sphere.

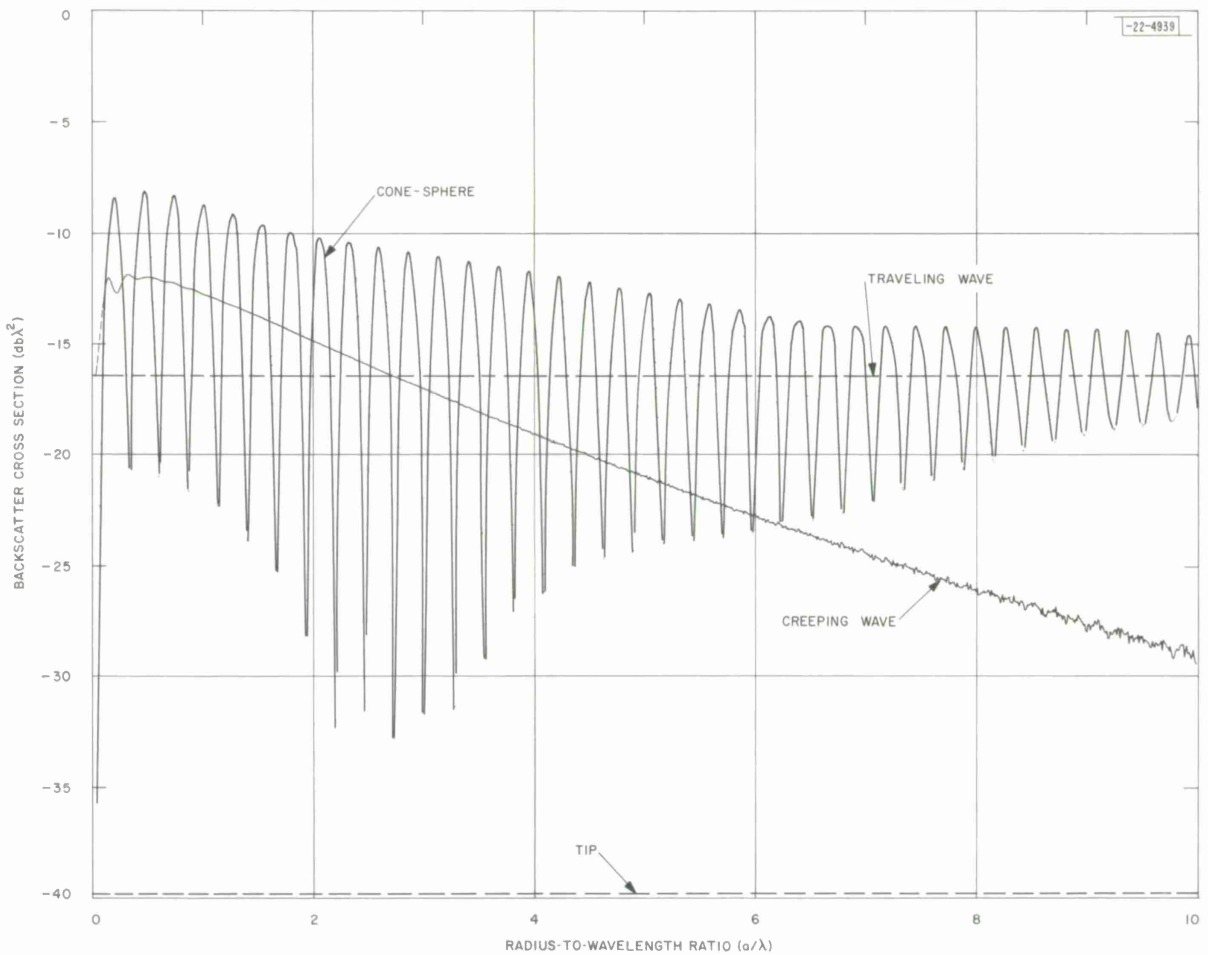

Fig. 26. Predicted nose-on backscatter cross section of a 15° half-angle cone-sphere. Also shown is the cross section due to each component as would be predicted if the other components were absent.

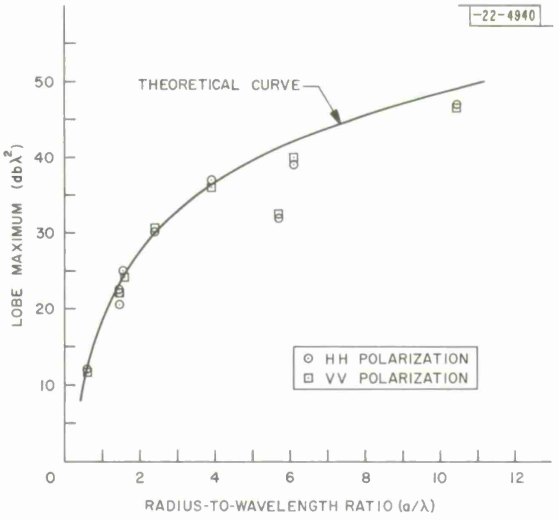

Fig. 27. Maximum amplitude of cone specular lobe.

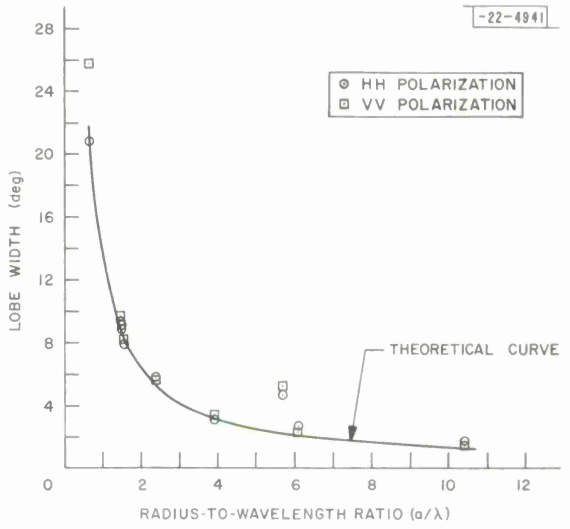

Fig. 28. Width of cone specular lobe.

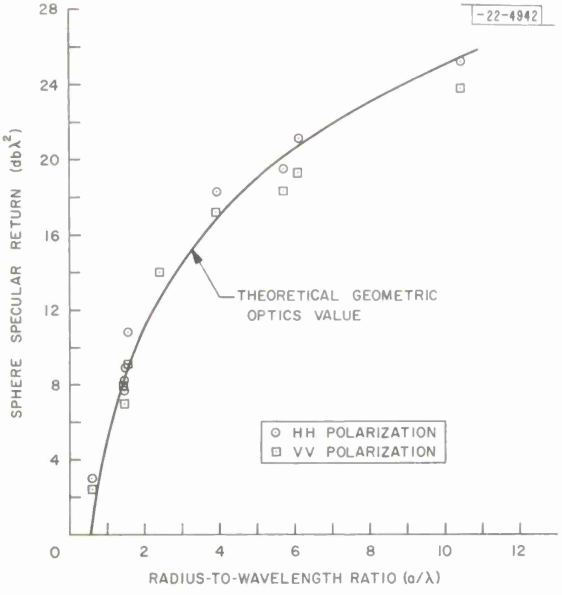

Fig. 29. Sphere specular return.